UC Berkeley
UC Berkeley Electronic Theses and Dissertations

Title

Microseismic event location with multiple arrivals: application in the Newberry Enhanced Geothermal System and the Marcellus Shale

Permalink
https://escholarship.org/uc/item/0xt5x2k6

Author

Zhang, Zhishuai

Publication Date

2017

Peer reviewed|Thesis/dissertation

eScholarship.org
Powered by the California Digital Library
University of California

Microseismic event location with multiple arrivals: application in the Newberry Enhanced Geothermal System and the Marcellus Shale

By

Zhishuai Zhang

A dissertation submitted in partial satisfaction of the

requirements for the degree of

Doctor of Philosophy

in

Engineering – Civil and Environmental Engineering

in the

Graduate Division

of the

University of California, Berkeley

Committee in charge:

Professor James W. Rector, Chair

Professor Steven D. Glaser

Professor Douglas S. Dreger

Spring 2017

Microseismic event location with multiple arrivals: application in the Newberry Enhanced Geothermal System and the Marcellus Shale

Copyright 2017

by

Zhishuai Zhang

ABSTRACT

Microseismic event location with multiple arrivals: application in the Newberry Enhanced Geothermal System and the Marcellus Shale

by

Zhishuai Zhang

Doctor of Philosophy in Civil and Environmental Engineering

University of California, Berkeley

Professor James W. Rector, Chair

Multistage fracturing technique, together with horizontal drilling, make production from organic-rich shale possible. Microseismic monitoring of hydraulic fractures has been an important technology for far-field fracture diagnostics. It can provide us hydraulic fracture geometry and its growth behavior vs. time. Getting accurate microseismic event location is important to interpretation. Various methods originally developed for earthquake location have been used for microseismic event location.

The main objective of this dissertation is to make use of multiple arrivals of microseismic data to improve microseismic event location accuracy. The improvement can be achieved from two aspect: (1) simultaneous inversion of multiple microseismic data for event locations and velocity model and (2) improving microseismic event location accuracy with head wave arrival time. We begin this dissertation by laying out the inverse problem theory as the basis of the simultaneous inversion. Then, we built a Bayesian framework to simultaneously invert for microseismic event locations and the velocity model. We developed a software package, BayesTomo, based on the simultaneous inversion framework.

The first application is the simultaneous inversion of microseismic event locations and the velocity in a microseismic survey at Newberry Enhanced Geothermal System (EGS). We successfully applied the developed method on both synthetic examples and real data from the Newberry EGS. Comparisons with location results based on a traditional predetermined velocity model method demonstrated that we can construct a reliable effective velocity model using only microseismic data and determine microseismic event locations without prior knowledge of the velocity model.

The second application is on the microseismic data acquired from a geophone array deployed in the horizontal section of a well drilled in the Marcellus Shale near Susquehanna County, Pennsylvania. We identified the existence of prominent head waves in some of the microseismic data. The head waves are refractions from the interface between the Marcellus and the underlying Onondaga Formation. The source locations of microseismic events can be significantly improved by using both the P-, S-wave direct arrival times and the head wave arrival times in place the traditional method of using direct arrival times and P-wave polarizations. The traditional method had substantially greater uncertainty in our data due to the large uncertainty in P-wave polarization direction estimation. Our method was applied to estimate the locations of perforation shots as well as microseismic events. Comparison with traditional location results shows improved location accuracy thanks to head wave arrival times.

To my wife, Bin Guo, and my parents, Guogui Zhang and Minhua Feng, for their support and love.

ACKNOWLEDGMENTS

I am deeply grateful to my advisor, Dr. James W. Rector, for his invaluable guidance and support throughout the course of my studies and research at UC Berkeley. Dr. Rector has the patience to help me grow from a student without any idea of the difference between elastic and acoustic waves to a PhD candidate in exploration geophysics. I am strongly influenced by his approaches to tackle research problems. It has been a great privilege for me to work with him and learn from his deep knowledge and expertise in the field of applied geophysics. This work would not have been possible without him.

I would like to thank Dr. Douglas S. Dreger from the Berkeley Seismological Laboratory whom I have taught alongside, has taught me a great deal about seismology, and served as a committee member. I would also like to thank my committee Dr. Steven D. Glaser, Dr. Nicholas Sitar, and Dr. Joan Bruna for their kind help and strong support during my PhD at UC Berkeley.

I thank my group members, Dr. Yang Zhao, Michael J. Nava, Hussain Jummah Alsalem, Nella Pierre Louis, Taqi Yousuf Alyousuf, Zheshu Wu, Dr. Yaping Huang, Dr. Christopher S. Sherman for their help and friendship during my PhD at UC Berkeley.

I was an exchange student at Stanford from January 2015 to March 2016. During this time, I gained a lot of knowledge on exploration geophysics by taking courses, working with fellow students, and attending group meetings at Stanford. I appreciate the help and support from professors and students of the Geophysics Department at Stanford.

I would also like to give special thanks to Dr. Jing Du and Dr. Fuchun Gao at Total E&P, Dr. Ali Tura at ConocoPhillips, and Mr. Jon Cocker at Chevron, and Dr. Denise Templeton at Lawrence Livermore National Laboratory for their tutoring and guidance during my internship. They provide me precious chance to apply my knowledge to real engineering practice and give me valuable advices on my career development.

I would like to gratefully acknowledge the Jane Lewis Fellowship Committee for their scholarship provision in the academic years 2014-2015 and 2015-2016 and

the Ning Fellowship Committee for their scholarship provision in the academic years 2012-2014. These scholarships greatly facilitated the continuation of my studies. I would also like to acknowledge the support from RPSEA under contract 11122-20 to my research.

Finally, I would like to give my deepest gratitude to my father, Guogui Zhang, my mother, Minhua Feng, and my lovely wife, Bin Guo for all of their support during my life. I love you forever.

TABLE OF CONTENTS

Abstract 1

Acknowledgments ii

Table of Contents iv

List of tables vii

List of figures viii

Chapter 1 Introduction 1

Chapter 2 Methodology 6

2.1 Inverse problem theory and its Gaussian approximation 6

2.1.1 Forward problem 6

2.1.2 Observation 7

2.1.3 Prior information 8

2.1.4 Inverse problem 9

2.2 Maximum a posteriori estimation 10

2.3 Simultaneous inversion for event locations and velocity model 11

Chapter 3 Application to Data from Newberry EGS 14

3.1 Microseismic survey in Newberry EGS system 14

3.1.1 Newberry EGS demonstration 15

3.1.2 Microseismic survey 15

3.2 Synthetic example 18

3.2.1 Gaussian random error 18

3.2.2 Velocity model parameterization error 24
3.3 Field data 25
3.4 Discussion 34
3.5 Conclusion 35
Chapter 4 Microseismic event location in the Marcellus Shale 37
4.1 Summary 37
4.2 Introduction 37
4.3 Hydraulic fracturing project overview 40
4.4 Data analysis 44
4.4.1 Spectrum of the resonance 46
4.4.2 Deconvolution of microseismic signal 47
4.4.3 Relative spectrum analysis 49
4.5 Head wave 51
4.5.1 Head waves 52
4.5.2 Velocity model calibration 55
4.5.3 Finite difference simulation 55
4.5.4 Perforation shot location 56
4.5.5 Relocation of events in the second stage 58
4.5.6 Acquisition geometry 59
4.6 Conclusions 63
Chapter 5 Conclusions 64
5.1 Discussions 64
5.2 Conclusions 65

5.3 Future work....66

References....68

LIST OF TABLES

Table 3-1: True, prior, and MAP estimated velocity model parameters and their associated standard deviations that represent uncertainties. 19

Table 4-1: Number of microseismic events in each stage. 43

LIST OF FIGURES

Figure 3-1: Map of surface stations and shallow borehole stations for microseismic monitoring. Surface stations provide complementary azimuthal coverage to the shallow borehole stations. The red dots indicate the locations of microseismic events. 16

Figure 3-2: Relative location of the seismic stations, well path, the open-hole portion of the well, and recorded microseismic events. The seismic stations provide good azimuthal coverage above the designed stimulation zone. 17

Figure 3-3: Histogram of the number of available picks for real data as well as for synthetic study. For stability purposes, we only studied the 179 events with at least eight picks available. 18

Figure 3-4: A two-layer velocity model was used for the synthetic study. Compared with the prior velocity model, the estimated model is much closer to the true velocity model. The simultaneous inversion successfully estimated the microseismic event locations. The estimation error in the vertical direction is larger than that in the horizontal direction. 20

Figure 3-5: The 90% confidence ellipsoids of the estimation in the synthetic study. The size of the ellipsoid increases as the depth of the event increases or as the number of available picks decreases. The uncertainty in the vertical direction is larger than that in the horizontal direction due to the limitation of the survey geometry. 22

Figure 3-6: The relationship between the theoretical prediction and the actual prediction confidence for the synthetic study with a Gaussian picking error. The Bayesian inference successfully predicted the location uncertainty of the estimation. 23

Figure 3-7: The estimated two-layer velocity model can capture the trend of the true multiple-layer model. It did not introduce significant error to the microseismic event locations. This shows that it is adequate to use a two-layer model in this specific scenario. 24

Figure 3-8: Comparison between our simultaneous location result and that provided by the contractor. The simultaneous location result is more clustered than the contractor's result. There is a significant difference in the lower boundaries of the shallow events for the contractor's result (around the elevation of 0 km) and our simultaneous inversion (around the elevation of 0.5 km) due to the difference in the velocity model. The simultaneously inverted P-wave velocity model is very close to the model obtained by seismic interferometry compared with the contractor’s model..26

Figure 3-9: The histogram of differences between the MAP estimated result and that provided by the contractor. The histogram in elevation differences has a broader distribution due to the larger location uncertainty in the vertical direction. The positive mean value of this distribution is mainly a result of the low Vp/Vs used by the contractor. 27

Figure 3-10: Velocity model estimated with two independent subsets of the data. The similarity between these two models verifies the stability of the simultaneous inversion..28

Figure 3-11: Velocity models estimated with microseismic events in various directions. The VP and Vp/Vs of the deeper layer are larger for the west and south event subsets. This may be caused by the dipping of the area downward to the southwest direction (Figure 3-1)...29

Figure 3-12: Correlation matrix of a deep event, a shallow event, and five velocity parameters. DE, the easting of the deep event; DN, the northing of the deep event; DEV, the elevation of the deep event; Dt, the occurrence time of the deep event; SE, the easting of the shallow event; SN, the northing of the shallow event; SEV, the elevation of the shallow event; St, the occurrence time of the shallow event; VR, velocity at the reference elevation of 1.5 km; VGu, velocity gradient of the upper layer; VGl, velocity gradient of the lower layer; IE, layer interface elevation; and PS, Vp/Vs. 30

Figure 3-13: The 90% confidence ellipsoids of the estimation of the field data. It shows a similar pattern with the synthetic case. Because the field data include random picking error and the velocity model parameterization error, the size of the confidence ellipsoids is larger than those in the synthetic case. 31

Figure 3-14: Comparison between picks, arrival times predicted by the contractor’s model, and arrival times predicted by simultaneous inversion. Simultaneous inversion was able to improve the match between the theoretical prediction and the real data. However, the improvement is not significant and we did not see a systematic change in the arrival time moveout, probability due to uncertainties resulting from sources other than the velocity model, such as statics. 32

Figure 3-15: Microseismic events color coded by their occurrence times. Early events only occur near the stimulation well. Late events can be either close to or far away from the stimulation well..33

Figure 3-16: Well head pressure, flow rate information, and the histogram (blue bins) of microseismic events. Microseismic events in the target zone only occur when the well head pressure is above approximately 1500 psi. 34

Figure 4-1: Microseismic survey geometry. The microseismic event locations (dots) were located conventionally using P-, S-wave arrival times and P-wave polarization directions. The geophone array is color-coded according to their locations. Microseismic events are color-coded according to their associated stimulation stages. 41

Figure 4-2: Map view of the acquisition geometry. The stimulation was performed in 18 stages and the microseismic signal was recorded by an array of 11 geophones in the nearby monitoring well. The geophone array was moved according to the stimulation stage location to reduce errors due to large event to receiver distances. 42

Figure 4-3: Waveforms of a typical perforation shot from stimulation stage 6. The source receiver distance is 0.31 km for geophone 1 and 0.22 km for geophone 11. The waveforms of a perforation shot are usually P-wave dominated due to the source mechanism of perforation shots. Severe resonance effect in waveforms can be observed, especially in the axial component (component 1). 45

Figure 4-4: Waveforms of a typical microseismic event from stimulation stage 6. The source receiver distance is 0.28 km for geophone 1 and 0.17 km for geophone 11. The waveforms of a microseismic event are usually S-wave dominated. 46

Figure 4-5: STFT of a typical three-component waveform generated by a perforation shot. For the axial component, the resonance frequency is around 420 Hz. The first radial component has resonance frequencies of 120 Hz and 440 Hz. And the second radial component resonates at 120 Hz and 340 Hz. The resonance around 120 Hz maybe be due the poor coupling between geophone and wellbohre. And the resonance around 400 Hz may result from the resonance of the geophone themselves. 47

Figure 4-6: Deconvolution result of the axial component. The source receiver distance is 0.31 km for geophone 1 and 0.22 km for geophone 11. The deconvolution successfully suppressed the resonance in the original data. In addition, it enhances multiple arrivals that are hardly identified in the original waveform...49

Figure 4-7: Single spectrum analysis (a and b) and relative spectrum analysis (c and d). The events are sorted according to the peak frequency of P-wave spectrum. The relative S-wave spectrum (d) shows a similar trend with P-wave spectrum (c). However, we cannot see this phenomenon from the single spectrum analysis. 51

Figure 4-8: The axial component of the waveforms of a perforation shot recorded by an array of geophones. The source receiver distance is 0.67 km for geophone 1 and 0.53 km for geophone 11. Head waves can be easily identified based on their low amplitude and high velocity moveout. 53

Figure 4-9: A common configuration for a head wave. Due to the low velocity nature of shale, the head wave is commonly identified when there is a nearby high velocity layer. 54

Figure 4-10: Arrival time of various phases as a function of source receiver distance. When source receiver distance is larger than the cross-over distance, the head wave can overtake the direct arrival to be the first arrival. Perforation 1 and Perforation 2 are respectively two perforation shots with source receiver distance larger and smaller than the cross-over distance. 54

Figure 4-11: Comparison between synthetic and real waveform. The synthetic waveform matches the real data relatively well, which verifies the existence of head wave. The difference between the S-wave in the x and y components may be due to the unknown source mechanism of the real event for simulation. 56

Figure 4-12： Comparison of estimated perforation shot locations and the true perforation locations. The perforation shot locations derived with P-, S-, and head waves is more accurate than the result using P-wave polarization as a constraint. 57

Figure 4-13: Map view of microseismic event locations processed using P-, S-wave arrival times and P-wave polarizations. The event location in stage 2 is much more scattered than those in later stages. 58

Figure 4-14: The microseismic event locations estimated with P-, S-, and head wave arrival times are less scattered when compared with the microseismic event locations processed using the traditional location method. 59

Figure 4-15: Waveforms of a typical perforation shot in stimulation stage 6. The source receiver distance is 0.29 km for geophone 1 and 0.21 km for geophone 11. This perforation shot is near the observation geophone array; thus, the head wave arrives after the direct P-wave arrival. Therefore, we cannot identify the head wave arrival in the waveform. 61

Figure 4-16: The locations of two perforation shots whose waveforms are shown by Figure 4-8 and Figure 4-15. 62

Figure 4-17: Traditional acquisition geometry aims at improving SNR by decreasing source receiver distance (red geophone array). Our study shows that one can monitor hydraulic stimulation with geophone array that is farther than a cross-over distance (yellow geophone array) for head wave observation. This acquisition practice will be able to avoid large location uncertainty due to using P-wave polarization. 62

CHAPTER 1 INTRODUCTION

Human activities, such as hydraulic fracturing, wastewater disposal, enhanced geothermal system (EGS) stimulation, and carbon sequestration, have been shown to induce small earthquakes. Microseismic analysis is the characterization of these small earthquakes for the purpose of monitoring subsurface human activities. The processing of microseismic data involves event location and, in some ideal circumstances, moment magnitude estimation and advanced source parameter and frequency analysis (Eisner and Le Calvez, 2007; Maxwell, 2014). Event location is the basis of almost all other advanced processing. It is a routine, yet in many circumstances, poorly understood, processing procedure in the microseismic industry. Existing methods for microseismic event location include least-squares traveltime inversion (Aki and Richards, 1980; Rutledge and Phillips, 2003), double-difference (Waldhauser and Ellsworth, 2000), coherence scanning (Drew et al., 2005; Duncan and Eisner, 2010), time-reverse imaging (Artman et al., 2010; Artman and Witten, 2011), and even full-waveform inversion (Song and Toksöz, 2011). Due to the often poor signal-to-noise ratio (S/N) of microseismic data, lack of information on velocity models, and limited spatial coverage of monitoring stations, microseismic location uncertainty can be significant (Eisner et al., 2009; Maxwell, 2009). Engineers without in-depth knowledge of microseismic processing might be confounded by the large uncertainty in event location (Hayles et al., 2011). As such, it is crucial to obtain a quantitative understanding of microseismic event location uncertainty before drawing any further conclusions on microseismic data. To improve acceptance of microseismic monitoring, geophysicists must address the following questions: (1) how to improve the absolute accuracy and relative precision of microseismic event location and (2) how to quantify the uncertainty associated with microseismic location estimation.

In microseismic processing, the velocity model is usually the most important factor in determining the accuracy and precision of microseismic event locations (Maxwell, 2009; Warpinski, 2009; Gesret et al., 2015). People typically obtain velocity information independently from microseismic data, such as from sonic logs, active-source surveys, or subsurface calibration/perforation shots. Depending on the availability of subsurface information, we can build a velocity model with various complexities such as heterogeneity and anisotropy (Grechka et al., 2011; Li et al., 2014) for microseismic processing. Moreover, rock properties may change during the treatment process, which requires a time-dependent subsurface velocity model (Tan et al., 2014). In a realistic survey, it can be challenging to build even a 1D velocity model. However, given the abundance of microseismic events in a normal survey, they are a good source of information to calibrate or even construct a velocity model for microseismic location estimation (Douglas, 1967).

Due to the importance of obtaining accurate velocity models in microseismic event location estimation, various studies have been carried out on simultaneous inversion for event locations and the velocity model (Zhang and Thurber, 2003; Zhang and Thurber, 2006; Jansky et al., 2010; Grechka, Singh and Das, 2011; Li et al., 2013; Li, Li, Morton, Dohmen, Katahara and Toksöz, 2014). Jansky, Plicka and Eisner (2010) study the feasibility of inverting for a 1D velocity model in various downhole monitoring geometries. Zhang and Thurber (2003); Zhang and Thurber (2006) develop a double-difference tomography method to improve velocity estimations with absolute and relative arrival times. It takes the absolute and relative arrival times into consideration and is successful on microseismic data (Zhang et al., 2009; Zhou et al., 2010). Li, Zhang, Rodi and Toksoz (2013) and Li, Li, Morton, Dohmen, Katahara and Toksöz (2014) estimate the Thomsen's parameters from microseismic data by assuming a vertical transverse isotropic model. Grechka, Singh and Das (2011) invert for the important anisotropic parameters by assuming a homogeneous velocity model in a downhole microseismic survey. These methods usually apply the traditional least-squares criterion for their inversions. In addition, they usually require determinations of weighting or regularization parameters, which can be challenging to estimate (Monteiller et al., 2005). Just as is typical with most inverse problems, the result can be highly dependent on the processor's subjectivity.

Bayesian inference is a widely used algorithm in subsurface inverse problems (Oliver et al., 2008; Zhang et al., 2014). Tarantola and Valette (1982) and Tarantola (2005) provide a general interpretation of Bayesian inference as a combination of states of information. They derive the statistical framework to combine prior information on model parameters, knowledge of the physical model, and information from observations into a joint probability density. Bayesian inference provides a good solution to earthquake (Monteiller (Monteiller, Got, Virieux and Okubo, 2005; Myers et al., 2007; Myers et al., 2009) and microseismic event location problems (Poliannikov et al., 2013; Poliannikov et al., 2014; Templeton et al., 2014; Zhang et al., 2015). Due to the fact that parameters are treated as a joint probability density, it has been very successful in model parameter estimation and uncertainty analysis. Compared with traditional methods of quantifying uncertainty (Eisner, Duncan, Heigl and Keller, 2009; Maxwell, 2009), Bayesian inference provides a more comprehensive way to take various sources of information into consideration. In addition, the application of Bayesian inference eliminates the necessity of various weighting parameters that are commonly required by a simultaneous inversion algorithm. Instead, it uses physically understandable parameters to describe the probability distribution of various parameters.

We apply Bayesian inference for simultaneous velocity inversion and event location using multiple microseismic event data. Tarantola (2005)'s interpretation of Bayesian inference provides the robustness of combining various sources of information in a statistical way. Thus, it makes uncertainty quantification in microseismic event location a straightforward process. With the help of simultaneous inversion, we can estimate effective velocity models for microseismic event locations using only microseismic data. This minimizes the efforts and expense required for a velocity survey. Successful applications of the developed method to synthetic and real microseismic surveys demonstrate its effectiveness. Furthermore, sensitivity analysis provides information on the source of event location uncertainty. As such, the result shows that we can successfully construct a velocity model using microseismic data and obtain reliable event locations without prior information on the velocity model.

For downhole microseismic monitoring, it is common to have only one nearby well available for microseismic monitoring (Warpinski, 2009). To assist in overcoming the aperture limitations imposed by the acquisition geometry, three-component geophones are deployed, which makes polarization analysis (Yuan and Li, 2016; Yuan et al., 2016) feasible. Moreover, multiple phase identification (Belayouni et al., 2015; Zhang, Rector and Nava, 2015), and full-waveform inversion (Song and Toksöz, 2011) of microseismic signal are also possible in some environments.

However, the coupling between geophones and the wellbore can be poor (J. Du, personal communication, 2016; J. Rector, personal communication, 2016). The poor coupling may lead to severe resonance in seismic waveform and is common in microseismic survey (J. Du, personal communication, 2016; J. Rector, personal communication, 2016). Gaiser et al. (1988) conducted an experiment to study the resonance of geophones in a vertical well used for vertical seismic profile (VSP). In their experiment, a geophone was locked in a vertical borehole with a horizontal locking force to imitate a typical VSP condition. They found the geophone was subject to severe resonance issues in the horizontal (radial) component that is perpendicular to the locking arm when the locking force is low. In the cases where the geophones are deployed in horizontal wells as common in microseismic monitoring, the situation is even worse since the only coupling force between the geophone and borehole is usually the gravitational force of the geophone itself. This, together with the unknown orientation of the downhole geophone, makes the microseismic signal analysis with three-component data extremely challenging. Bandpass filters have been designed and applied in previous research to mitigate the effect of downhole geophone resonance (Nava et al., 2015); however, this is based on the assumption that the resonance frequency is known and different from microseismic spectrum.

Microseismic surveys with a single monitoring well and with only P- and S-wave arrival times result in event locations with ambiguity due to the limited coverage of acquisition geometry. An additional constraint on event location usually comes from direct P-wave polarization (Dreger et al., 1998; Eisner, Duncan, Heigl and Keller, 2009; Li, Li, Morton, Dohmen, Katahara and Toksöz, 2014). Three-component data are necessary for P-wave polarization direction estimation. The major challenges in using three-component data are the unknown orientation of downhole geophones, poor coupling between geophone and borehole wall, and anisotropic/multiple arrival effects in the P-wave polarization estimation. When there are near horizontal raypaths between treatment and monitor wells, arrivals travelling in high velocity layers can affect the polarization estimation of the direct arrival. Perforation shots can be used for geophone orientation calibration. However, depending on the stimulation design, perforation may not have been conducted or recorded by the geophones. These challenges make the uncertainty in the P-wave polarization estimation relatively large, and is usually a major source of microseismic event location uncertainty (Eisner, Duncan, Heigl and Keller, 2009; Maxwell, 2009).

When the seismic source and receiver are both located at nearly the same depth in low velocity shale, head wave arrivals can often be observed. There are numerous examples in the crosswell (Dong and Toksöz, 1995; Parra et al., 2002; Parra et al., 2006) and microseismic (Maxwell, 2010; Zimmer, 2010; Zimmer, 2011) literature where the head wave arrival is the first arrival. People have realized the possible presence of head wave before direct arrival. However, due to its weakness, it has been commonly regarded as contamination of the direct arrival. Synthetic study on making use of head waves has been conducted (Zimmer, 2010; Zimmer, 2011), however, there are few studies using field data on the improvement in event location obtained by using available head waves. Our analysis on microseismic data acquired in the Marcellus shale shows that head waves convey useful information, and can be used to constrain microseismic event location as a substitution for the P-wave polarization.

CHAPTER 2 METHODOLOGY

In this chapter, we present the formulation and solution of simultaneous inversion as a Bayesian inference problem. Here, the central idea is to represent all the information we have (forward model, observation, and prior information) with probability densities. Then, using inverse theory, we infer the posterior probability density of the model parameters we would like to know. We define observations as the information we have from a survey and would like to use to improve knowledge of model parameters. Likewise, prior information is defined as what we know about model parameters from knowledge other than the studied survey. Finally, the forward model serves as the link between model parameters (the information we want to know) and observations (the information we have from a survey).

2.1 Inverse problem theory and its Gaussian approximation

Tarantola (2005) provided the interpretation of Bayesian inference as a combination of information. Here, we give an overview of his derivation and the form of inverse problem theory under Gaussian approximation.

2.1.1 Forward problem

Solving inverse problem using Bayesian inference requires knowledge on the forward problem. Every physical theory has accompanying uncertainty. This can be a result of parameterization, basic knowledge of the physical process, or simplification of the model. To address uncertainties, we are going to use a stochastic model instead of a deterministic model to describe the forward physical theory.

The forward problem can be described by $\Theta(\mathrm{d}, \mathrm{m})$, which is a joint probability density for a given pair of data d and model parameters m based the physical theory and confidence we have on the forward problem. The joint probability density can be expressed as the product of conditional probability density and marginal probability density. If the marginal probability density of the model parameters is homogeneous, we arrive at the joint probability density:

$$\Theta(\mathrm{d},\mathrm{m}) = \theta(\mathrm{d}|\mathrm{m})\mu_M(\mathrm{m}), \tag{2.1}$$

where $\Theta(\mathrm{d},\mathrm{m})$ is the conditional probability density of data d given model parameters m. In other words, given any input parameter m (seismic event location, occurrence time, and velocity model), instead of predicting an exact measurable data d (arrival time and/or polarization at each station), the forward modeler will give a probability density of the measurable data d due to the uncertainty of the forward modeler. The homogeneous probability density $\mu_M(\mathrm{m})$ is constant for linear data space.

To simplify the problem, we assume the theoretical uncertainty (uncertainty of the forward modeler) is Gaussian. Under this assumption, the conditional probability distribution can be expressed as

$$\theta(\mathrm{d}|\mathrm{m}) = c_1\left\{-\frac{1}{2}[\mathrm{d}-\mathrm{g}(\mathrm{m})]^{\mathrm{T}}\mathrm{C}_{\mathrm{T}}^{-1}[\mathrm{d}-\mathrm{g}(\mathrm{m})]\right\}, \tag{2.2}$$

where the Gaussian covariance matrix C_{T} describes the theoretical uncertainty of our forward modeler, and $\mathrm{g}(\cdot)$ is a function of the model parameters m that will give a prediction of the measurable data d. And c_1, as well as c_2, c_3, c_4, c_5 and c_6 in the following, is a constant. Thus, the joint probability density is

$$\Theta(\mathrm{d}|\mathrm{m}) = c_1\left\{-\frac{1}{2}[\mathrm{d}-\mathrm{g}(\mathrm{m})]^{\mathrm{T}}\mathrm{C}_{\mathrm{T}}^{-1}[\mathrm{d}-\mathrm{g}(\mathrm{m})]\right\}\mu_M(\mathrm{m}). \tag{2.3}$$

2.1.2 Observation

Any measurement has unavoidable uncertainty. The uncertainty in the process of phase picking can be a result of precision of measurement instruments (seismometers or geophones) and the subjectivity of the phase picker. Due to the low S/N in microseismic observation, it may result in a large uncertainty in the determination of arrival time. We can express the information obtained from a measurement as a probability density in data space $\rho_D(\mathrm{d})$.

If the data space is linear, it is proportional to the conditional probability density:

$$\rho_{\mathrm{D}}(\mathrm{d}) = c_2 \nu(\mathrm{d}_{\mathrm{obs}}|\mathrm{d}), \tag{2.4}$$

where $\mathrm{d}_{\mathrm{obs}}$ is the measurement on observable parameters.

A further Gaussian assumption gives a specific form:

$$\rho_{\mathrm{D}}(\mathrm{d}) = c_3 \left[-\frac{1}{2}(\mathrm{d} - \mathrm{d}_{\mathrm{obs}})^{\mathrm{T}} \mathrm{C}_{\mathrm{d}}^{-1} (\mathrm{d} - \mathrm{d}_{\mathrm{obs}})\right]. \tag{2.5}$$

The covariance matrix C_{d} describes the uncertainty in measurement (uncertainty due to the seismometer and the subjectivity of the picker).

2.1.3 Prior information

The prior information is the information on model parameters m we have independent of the measurement we are going to use for the inversion, such as the initial guess of microseismic event locations, or the information on velocity model we get from an active geophysical survey. We can represent the prior information as a probability density $\rho_{\mathrm{M}}(\mathrm{m})$. If we have no prior information, we can use a homogenous probability density as the prior information:

$$\rho_{\mathrm{M}}(\mathrm{m}) = \mu_M(\mathrm{m}). \tag{2.6}$$

Similar to our treatment on measurement, we can describe the prior information with a Gaussian distribution. In this case, we will have

$$\rho_{\mathrm{M}}(\mathrm{m}) = c_4 \left[-\frac{1}{2}\left(\mathrm{m} - \mathrm{m}_{\mathrm{prior}}\right)^{\mathrm{T}} \mathrm{C}_{\mathrm{M}}^{-1} \left(\mathrm{m} - \mathrm{m}_{\mathrm{prior}}\right)\right]. \tag{2.7}$$

where $\mathrm{m}_{\mathrm{prior}}$ is the prior information we have on model parameters and C_{M} is the uncertainty matrix of them.

2.1.4 Inverse problem

After having all the information on the forward model, measurement, and the prior information, we can combine them to give the posterior information with a probability density:

$$\begin{aligned}\sigma(\mathrm{d},\mathrm{m}) &= c_5\frac{\rho(\mathrm{d},\mathrm{m})\Theta(\mathrm{d},\mathrm{m})}{\mu(\mathrm{d},\mathrm{m})} = c_5\frac{\rho_{\mathrm{D}}(\mathrm{d})\rho_{\mathrm{M}}(\mathrm{m})\theta(\mathrm{d}|\mathrm{m})\mu_{\mathrm{M}}(\mathrm{m})}{\mu_{\mathrm{D}}(\mathrm{d})\mu_{\mathrm{M}}(\mathrm{m})} \\ &= c_5\frac{\rho_{\mathrm{D}}(\mathrm{d})\rho_{\mathrm{M}}(\mathrm{m})\theta(\mathrm{d}|\mathrm{m})}{\mu_{\mathrm{D}}(\mathrm{d})}.\end{aligned} \tag{2.8}$$

The objective of our inverse problem is finding the marginal probability density of m. It is the integration of the joint probability density over the entire data space $\mathfrak{D}$:

$$\sigma_M(\mathrm{m}) = \int_{\mathfrak{D}} d\mathrm{d}\,\sigma(\mathrm{d},\mathrm{m}). \tag{2.9}$$

Based on Tarantola (2005)'s demonstration, if the model and data space are both linear, under Gaussian assumption, the posterior probability density of the model parameters can be expressed by

$$\begin{aligned}\sigma_M(\mathrm{m}) = c_6\Big\{&-\frac{1}{2}[\mathrm{g}(\mathrm{m})-\mathrm{d}_{\mathrm{obs}}]^{\mathrm{T}}\mathrm{C}_{\mathrm{D}}^{-1}[\mathrm{g}(\mathrm{m})-\mathrm{d}_{\mathrm{obs}}] \\ &-\frac{1}{2}\left(\mathrm{m}-\mathrm{m}_{\mathrm{prior}}\right)^{\mathrm{T}}\mathrm{C}_{\mathrm{M}}^{-1}\left(\mathrm{m}-\mathrm{m}_{\mathrm{prior}}\right)\Big\},\end{aligned} \tag{2.10}$$

where $\mathrm{C_D} = \mathrm{C_d} + \mathrm{C_T}$ is the addition of observation uncertainty and model uncertainty covariance matrices.

2.2 Maximum a posteriori estimation

Even if all the information we have are of the Gaussian type, as a result of the nonlinear operator $\mathrm{g}(\cdot)$, the posterior probability density may take a more complex non-Gaussian form (Oliver et al., 1996) that, in general, is difficult to be predicted. Two general approaches are considered in the literature for characterizing the resulting posterior probability density. The first approach aims to estimate statistics of the posterior probability density, such as its mean and covariance, which provide incomplete, yet important, characterization of the conditional parameter distribution. The second approach focuses on approximating the posterior probability density by generating many conditional realizations that enable a systematic approach to uncertainty quantification, such as Markov chain Monte Carlo (MCMC). In this study, we use the maximum a posteriori estimation and its posterior covariance approximation under a Gaussian assumption, which lies in the first category, to characterize the model parameters.

The MAP estimation aims at finding the mode of the posterior probability density $\sigma_M(\mathrm{m})$:

$$\mathrm{m_{MAP}} = \arg\max_{\mathrm{m}} \sigma_M(\mathrm{m}). \tag{2.11}$$

Or equivalently minimizes

$$\begin{aligned} O(m) = {} & \frac{1}{2}[\mathrm{g(m)} - \mathrm{d_{obs}}]^{\mathrm{T}}\mathrm{C_D^{-1}}[\mathrm{g(m)} - \mathrm{d_{obs}}] \\ & + \frac{1}{2}\left(\mathrm{m} - \mathrm{m_{prior}}\right)^{\mathrm{T}}\mathrm{C_M^{-1}}\left(\mathrm{m} - \mathrm{m_{prior}}\right). \end{aligned} \tag{2.12}$$

The above minimization can be implemented using a Gauss-Newton method (Oliver, Reynolds and Liu, 2008; Li and Jafarpour, 2010). By taking the derivative of the objective function with respect to m and rearranging, we obtain

$$\begin{aligned} \mathrm{m}^{\mathrm{n}+1} = {} & \left[\left(\mathrm{C}_{\mathrm{M}}^{-1} + \mathrm{C}_{\mathrm{M}}^{-1^{\mathrm{T}}}\right) + \mathrm{G}^{\mathrm{nT}}\left(\mathrm{C}_{\mathrm{D}}^{-1} + \mathrm{C}_{\mathrm{D}}^{-1^{\mathrm{T}}}\right)\mathrm{G}^{\mathrm{n}}\right]^{-1} \\ & \times\left\{\left(\mathrm{C}_{\mathrm{M}}^{-1} + \mathrm{C}_{\mathrm{M}}^{-1^{\mathrm{T}}}\right)\mathrm{m}_{\mathrm{prior}} \right. \\ & \left. + \mathrm{G}^{\mathrm{nT}}\left(\mathrm{C}_{\mathrm{D}}^{-1} + \mathrm{C}_{\mathrm{D}}^{-1^{\mathrm{T}}}\right)\left[\mathrm{d}_{\mathrm{obs}} - \mathrm{g}(\mathrm{m}^{\mathrm{n}}) + \mathrm{G}^{\mathrm{n}}\mathrm{m}^{\mathrm{n}}\right]\right\}. \end{aligned} \tag{2.13}$$

where G is the sensitivity matrix with elements $\mathrm{G}_{\mathrm{ij}} = \frac{\partial g_i}{\partial m_j}$. Once the MAP estimate $\mathrm{m}_{\mathrm{MAP}}$ is found, the posterior covariance matrix $\mathrm{C}_{\mathrm{m,MAP}}$ can be approximated through linearization about the MAP estimate (Tarantola, 2005) as

$$\mathrm{C}_{\mathrm{m,MAP}} = \mathrm{C}_{\mathrm{M}} - \mathrm{C}_{\mathrm{M}}\mathrm{G}_{\mathrm{MAP}}^{\mathrm{T}}\left(\mathrm{G}_{\mathrm{MAP}}\mathrm{C}_{\mathrm{M}}\mathrm{G}_{\mathrm{MAP}}^{\mathrm{T}} + \mathrm{C}_{\mathrm{D}}\right)^{-1}\mathrm{G}_{\mathrm{MAP}}\mathrm{C}_{\mathrm{M}}. \tag{2.14}$$

Or equivalently,

$$\mathrm{C}_{\mathrm{m,MAP}} = \left(\mathrm{G}_{\mathrm{MAP}}^{\mathrm{T}}\mathrm{C}_{\mathrm{D}}^{-1}\mathrm{G}_{\mathrm{MAP}} + \mathrm{C}_{\mathrm{M}}^{-1}\right)^{-1}. \tag{2.15}$$

Equation (2.14) is more computationally efficient for high-dimensional models.

2.3 Simultaneous inversion for event locations and velocity model

The implementation of the inversion method developed above in the simultaneous estimation of event locations and the velocity model includes the definition of model parameters, prior information on model parameters, measurement, and the forward model.

Ideally, the model should include all the uncertainty parameters that have large impacts on the prediction of the observable parameters. On the other hand, a model space with too large a dimension may cause the inverse problem to be ill-posed. The velocity model we use in this study is a two-layer model with a constant velocity gradient for each layer. The velocity model parameters to be estimated include the P-wave velocity at a reference elevation, P-wave velocity gradient for each of the two layers, the elevation of the two-layer interface, and V_P/V_S. Specifically, for a system with N microseismic events, the model parameter m is a vector of length $4N + 5$, including the space and time coordinate $[x, y, z, t_o]^T$ for each event and the five parameters for velocity model characterization.

Normally, we have very limited prior information on microseismic event locations and occurrence times before inversion. Therefore, we can use any reasonable locations along with a relatively large uncertainty to approximate a homogeneous probability density. For prior information on the velocity model, we can use prior information from other independent geophysical surveys with its corresponding uncertainty. Alternatively, we can even use a homogeneous probability density because we can parameterize the earth model with a minimum number of essential parameters so that the model can be determined purely using the microseismic events' arrival-time information.

Measurements include any available P- and/or S-wave arrival times for each event at each station. Because the observations of arrival times at various stations for these events are made individually, we will assume that there is no correlation between various observations, and thus covariance matrix Cd becomes a diagonal matrix with variance at corresponding diagonal positions. The determination of theoretical uncertainty covariance matrix CT requires specific analysis of the model itself. We will give a preliminary analysis of this with a synthetic example in the next section.

The forward model calculates the arrival time from the microseismic event location to a receiver location. The raypaths in a constant gradient model can be obtained analytically (Slawinski and Slawinski, 1999).We solve the two-layer problem semianalytically by iterating for the ray parameter that is common to the seismic rays in both layers.

CHAPTER 3 APPLICATION TO DATA FROM NEWBERRY EGS

In this chapter, we have applied Bayesian inference for simultaneous inversion of multiple microseismic data to obtain event locations along with the subsurface velocity model. The traditional method of using a predetermined velocity model for event location may be subject to large uncertainties, particularly if the prior velocity model is poor. Our study indicated that microseismic data can help to construct the velocity model, which is usually a major source of uncertainty in microseismic event locations. The simultaneous inversion eliminates the requirement for an accurate predetermined velocity model in microseismic event location estimation. We estimate the posterior probability density of the velocity model and microseismic event locations with the maximum a posteriori estimation, and the posterior covariance approximation under the Gaussian assumption. This provides an efficient and effective way to quantify the uncertainty of the microseismic location estimation and capture the correlation between the velocity model and microseismic event locations. We have developed successful applications on both synthetic examples and real data from the Newberry enhanced geothermal system. Comparisons with location results based on a traditional predetermined velocity model method demonstrated that we can construct a reliable effective velocity model using only microseismic data and determine microseismic event locations without prior knowledge of the velocity model.

3.1 Microseismic survey in Newberry EGS system

We applied the developed simultaneous inversion algorithm to synthetic and real data from the Newberry EGS demonstration site (Petty et al., 2013). Fluid injection for hydroshearing site (Petty, Nordin, Glassley, Cladouhos and Swyer, 2013) has induced microseismic events in this area. A contractor conducted an active-source seismic survey to determine a 1D velocity model for microseismic event location. Event locations were estimated by the contractor using picked P- and S-wave arrival times. With the same picked arrival times, we relocated the microseismic events using our simultaneous inversion approach. The analysis of the inversion result shows that the simultaneous inversion is able to construct an effective velocity model by matching the observed arrival times of microseismic events. It also demonstrates the robustness of our algorithm over the traditional location method, which requires a predetermined velocity model.

3.1.1 Newberry EGS demonstration

The EGS system under study is located at the Newberry volcano in Central Oregon. According to the stimulation plan (Osborn et al., 2011; Petty, Nordin, Glassley, Cladouhos and Swyer, 2013), an existing well, NGC 55-29, was stimulated with a hydroshearing technique due to the high temperature and lack of permeability of the nearby formation. Well NGC 55-29 has a total depth of 3066 m with an open hole from 1790 m to its total depth. In contrast to well-known hydraulic fracturing, the hydroshearing technique used in this demonstration stimulated the formation below its minimum principal stress. The stimulation induced shear failures of preexisting natural fractures in the target formation. This process was monitored with seismometers on the surface and in shallow boreholes. After the completion of the stimulation, two production wells will be drilled based on microseismicity clouds generated during stimulation of the injection well, NGC 55-29. These three wells will form a circulation system for long-term testing and performance assessment.

3.1.2 Microseismic survey

The survey was conducted with 15 seismic stations, which include seven seismometers placed on the surface and eight placed in shallow boreholes as shown in Figure 3-1. A permitting issue led to poor azimuthal coverage of the shallow borehole stations. However, surface stations provide complementary coverage. Eight shallow monitoring holes were drilled to depths between 213 and 246 m. A primary objective is to reach below the water table and the highly attenuating cinders and debris flows (Cladouhos et al., 2013). The stimulation of NGC 55–29 began on 17 October 2012 and went until 7 December 2012, and the first detected microseismic event occurred on 29 October. A total of 204 events with reasonably high S/Ns were recorded until 31 December 2012. Figure 3-2 provides a 3D view of the relative location of the seismic stations, the well path, the open-hole portion of the well, and the recorded microseismic events.

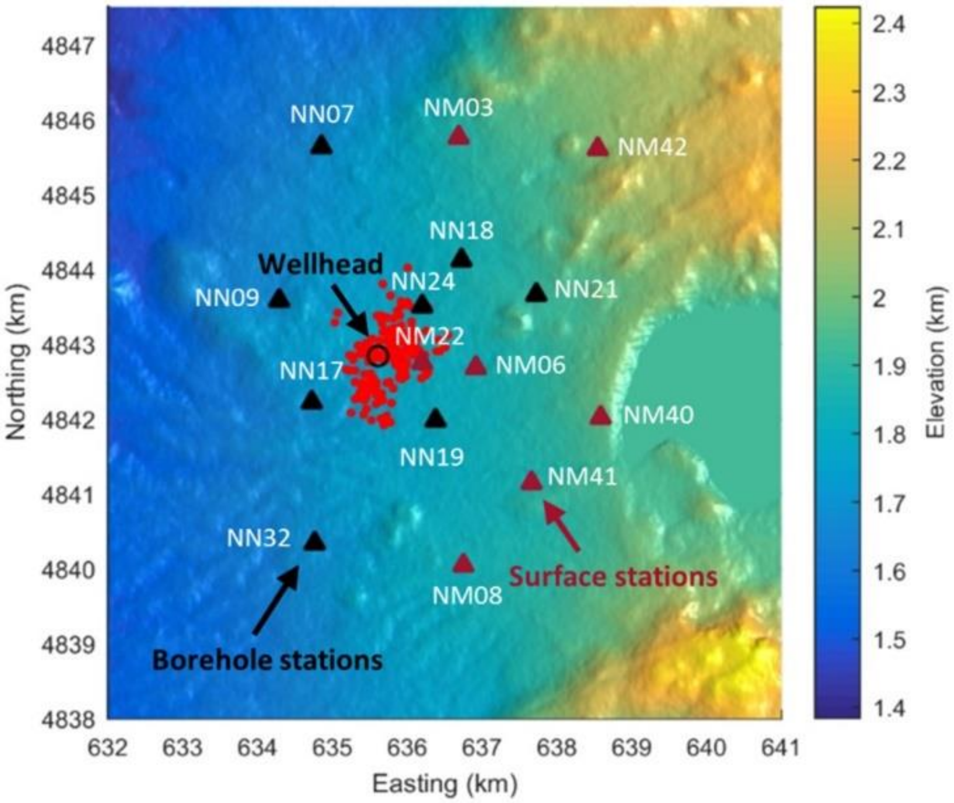
NN07
NM03
NM42
NN18
Wellhead
NN24
NN21
NN09
NM22
NM06
NN17
NM40
NN19
NM41
NN32
Surface stations
NM08
Borehole stations
Northing (km)
4847
4846
4845
4844
4843
4842
4841
4840
4839
4838
Easting (km)
632
633
634
635
636
637
638
639
640
641
Elevation (km)
2.4
2.3
2.2
2.1
2
1.9
1.8
1.7
1.6
1.5
1.4

Figure 3-1: Map of surface stations and shallow borehole stations for microseismic monitoring. Surface stations provide complementary azimuthal coverage to the shallow borehole stations. The red dots indicate the locations of microseismic events.

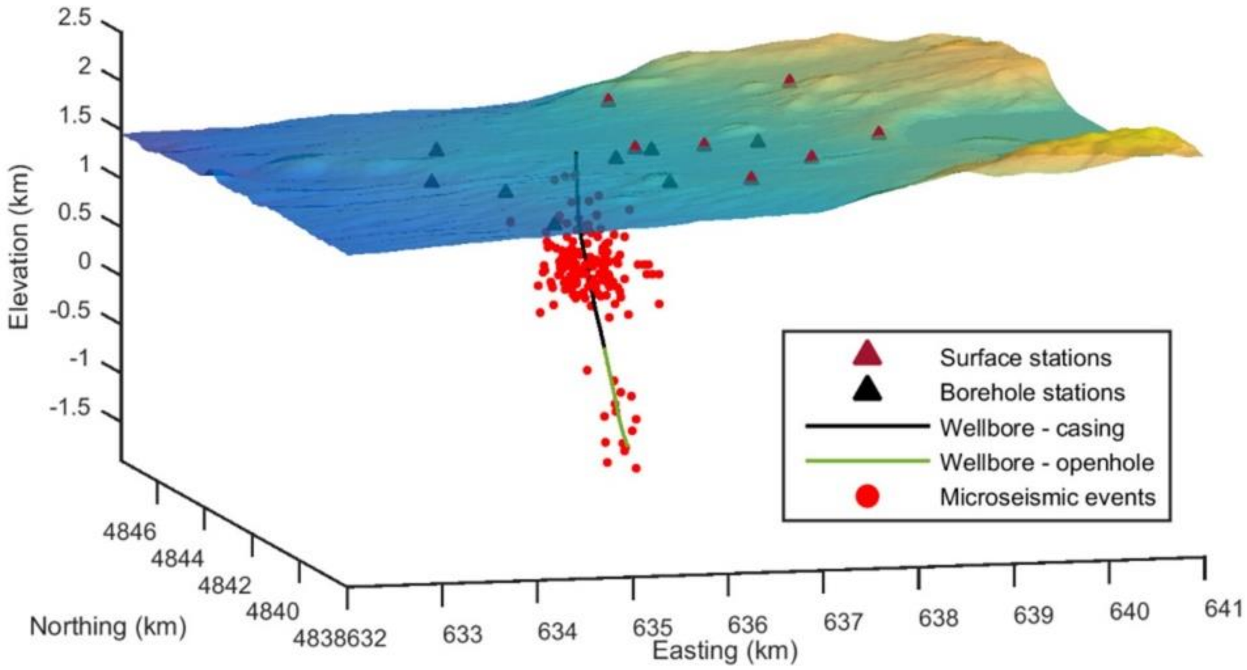

Figure 3-2: Relative location of the seismic stations, well path, the open-hole portion of the well, and recorded microseismic events. The seismic stations provide good azimuthal coverage above the designed stimulation zone.

To process the microseismic data set, the contractor has picked P- and/or S-wave arrival times for all event-station pairs whenever possible. To ensure the stability of the inversion, we only used events with at least eight picks available, which leaves 179 out of 204 events to meet this criterion. The histogram of the number of available picks for these 179 events is shown in Figure 3-3. The contractor also derived a 1D velocity model by conducting a dedicated active-source seismic survey. With the obtained velocity model, they located the microseismic events by minimizing the misfit between the observed and modeled P- and/or S-wave arrival times. A velocity model constructed by Matzel et al. (2014) with interferometry is also used for comparison.

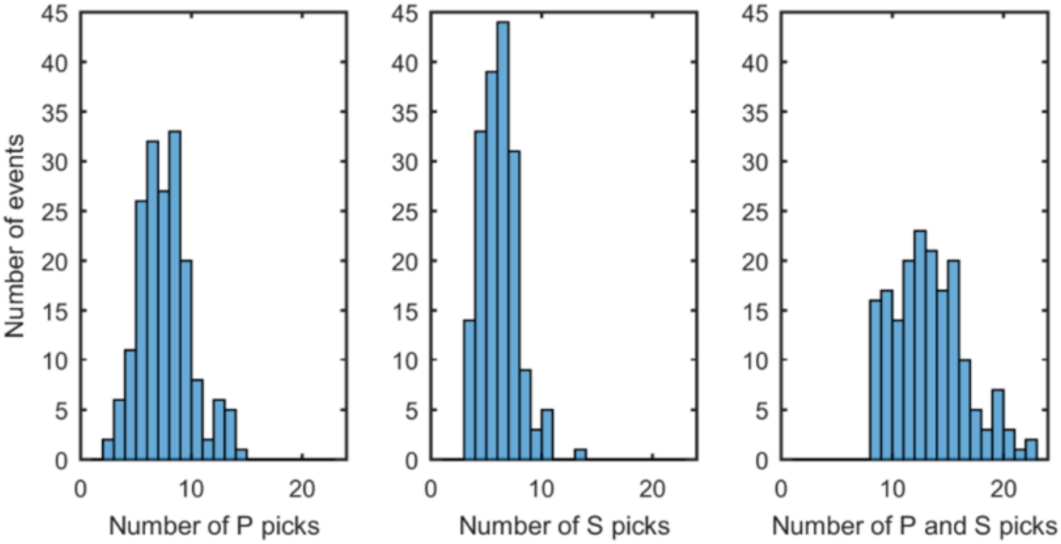

Figure 3-3: Histogram of the number of available picks for real data as well as for synthetic study. For stability purposes, we only studied the 179 events with at least eight picks available.

3.2 Synthetic example

First, we studied a synthetic model with the same acquisition geometry as the field survey. The histograms of the number of available picks for all the 179 events are the same as the field data shown in Figure 3-3.

3.2.1 Gaussian random error

The first experiment is to study the effect of Gaussian random errors on event locations and velocity model estimation. We assume that the velocity model has the potential to characterize the true model perfectly. That is, the theoretical uncertainty covariance matrix C_T is zero. To achieve this goal, we use a two-layer velocity model for the synthetic data set construction and the inversion. Five variables can completely characterize this velocity model: the P-wave velocity at a reference elevation (fixed at 1.5 km in this study), velocity gradient of the upper layer, velocity gradient of the lower layer, elevation of the two layer interface, and Vp/Vs. The true values used for forward modeling are in the first column of Table 3-1. The velocity model represented by these parameters is the red line in Figure 3-4.

Table 3-1: True, prior, and MAP estimated velocity model parameters and their associated standard deviations that represent uncertainties.

Parameter	True value	Prior mean	Prior SD	MAP value	Posterior SD
Reference elevation (km)	1.50 (fixed)				
Reference velocity (km/s)	2.46	2.00	1.00	2.47	0.03
Upper gradient (1/s)	2.76	1.50	2.00	2.80	0.07
Lower gradient (1/s)	0.74	1.50	2.00	0.78	0.02
Interface elevation (km)	1.07	0.80	0.50	1.10	0.04
Vp/Vs	1.72	1.65	0.25	1.72	0.00

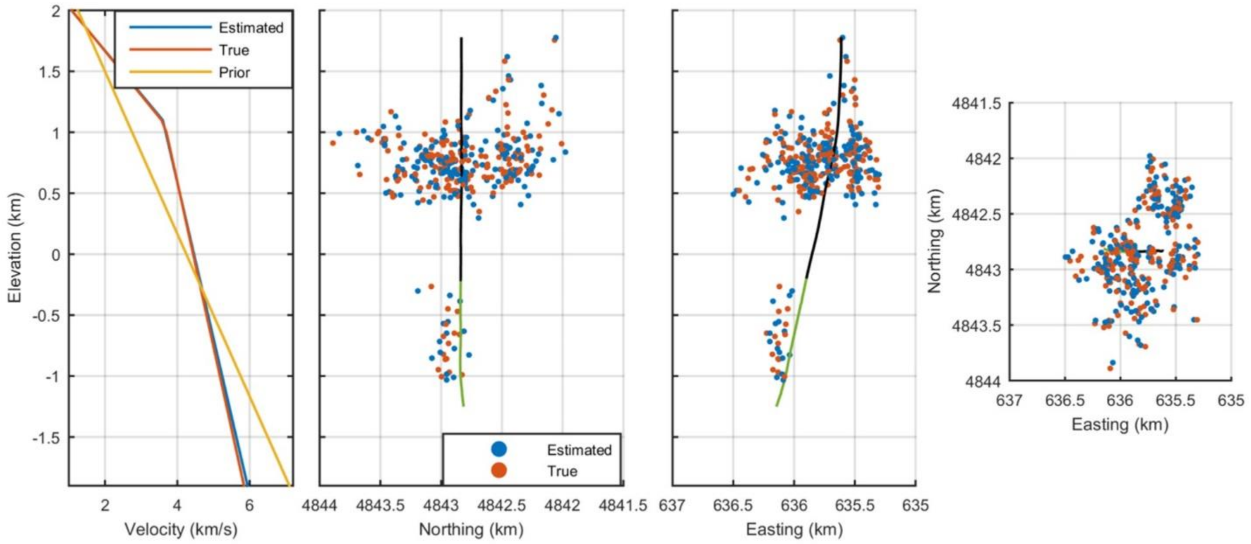

Figure 3-4: A two-layer velocity model was used for the synthetic study. Compared with the prior velocity model, the estimated model is much closer to the true velocity model. The simultaneous inversion successfully estimated the microseismic event locations. The estimation error in the vertical direction is larger than that in the horizontal direction.

The P- and S-wave traveltimes are calculated semianalytically for each event-station pair, and a Gaussian noise with standard deviation (SD) of 0.022 s is added as a representation of random error. We assume that there is little prior information on the microseismic event locations and velocity model parameters. A multivariate normal distribution with reasonable mean and sufficiently large standard deviation can approximate a homogeneous probability density for prior information and the initial model. Prior mean values and standard deviations of the velocity model parameters are listed in columns 2 and 3 of Table 3-1. The corresponding velocity model is represented by the yellow line in Figure 3-4. A comparison between true microseismic locations and the estimated locations is also shown in Figure 3-4, and the estimated 90% confidence ellipsoids are shown in Figure 3-5. The size of the error ellipsoids mainly depends on two factors: the number of available picks and the location of an event. The size of the error ellipsoids will decrease as the number of available picks increases. As an event goes deeper, its location uncertainty will become larger. In addition, we observed that the vertical location uncertainty is larger than the horizontal uncertainty, which is commonly known for surface-acquired microseismic data (Eisner, Duncan, Heigl and Keller, 2009). To verify the effectiveness of the MAP estimation and uncertainty approximation, we calculated the error ellipsoids of the estimation from 10% to 90% at a 10%

interval. Then, for ellipsoids corresponding to each error value, we counted the ratio of locations estimated within the predicted ellipsoids as the actual estimation confidence. Its relation with the predicted confidence with Equation (2.14) or (2.15) is shown in Figure 3-6. The match between these two confidences verifies the effectiveness of the MAP estimation and the uncertainty approximation.

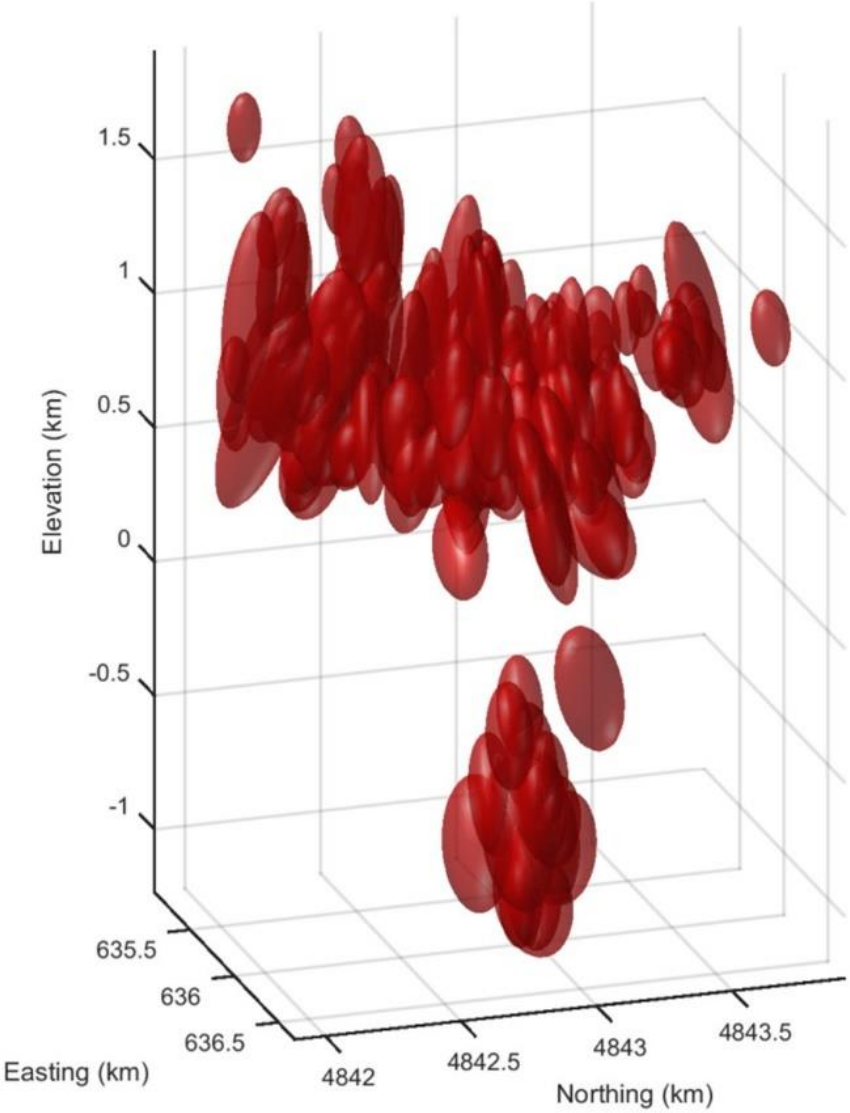

Figure 3-5: The 90% confidence ellipsoids of the estimation in the synthetic study. The size of the ellipsoid increases as the depth of the event increases or as the number of available picks decreases. The uncertainty in the vertical direction is larger than that in the horizontal direction due to the limitation of the survey geometry.

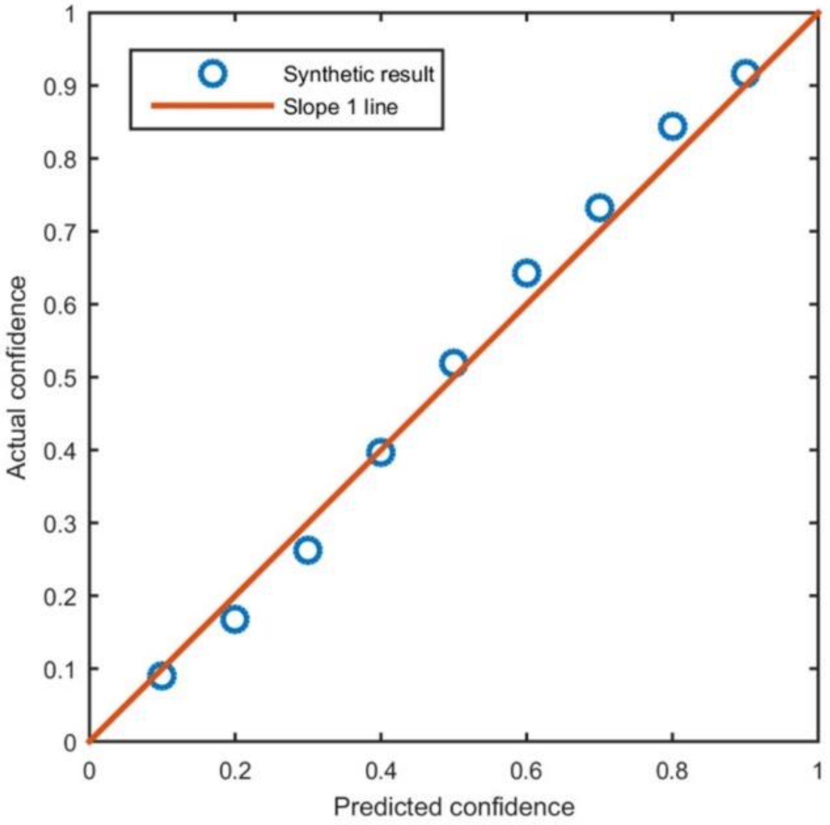

Figure 3-6: The relationship between the theoretical prediction and the actual prediction confidence for the synthetic study with a Gaussian picking error. The Bayesian inference successfully predicted the location uncertainty of the estimation.

The MAP estimation of velocity model parameters and their uncertainties are also shown in Table 1 and the blue line in Figure 3-4. We can see from the result that the velocity model can be successfully recovered by simultaneous inversion using multiple microseismic data. The MAP values of the velocity model parameters are much closer to the true values compared with the prior estimates. In addition, the standard deviations of the posterior probability distribution are good representations of the deviations of the MAP values. This verifies the effectiveness of the Bayesian inference for our multiple events location problem.

3.2.2 Velocity model parameterization error

The two-layer velocity model seems oversimplified at first glance. However, our study in this subsection shows that it is possible to characterize a multiple-layer model, which has more parameters that may cause unstable inversion with a two-layer velocity model. In this synthetic example, the velocity model used for data set construction is a multiple-layer model based on Matzel, Templeton, Petersson and Goebel (2014)'s interferometry estimation at the Newberry EGS site (the red line in Figure 3-7). Because the purpose of this section is to study the velocity parameterization error CT introduced by a two-layer velocity model, no picking error was added to the forward modeling result. That is, $\mathrm{C_d}$ is zero. All other parameters stay the same as the previous section.

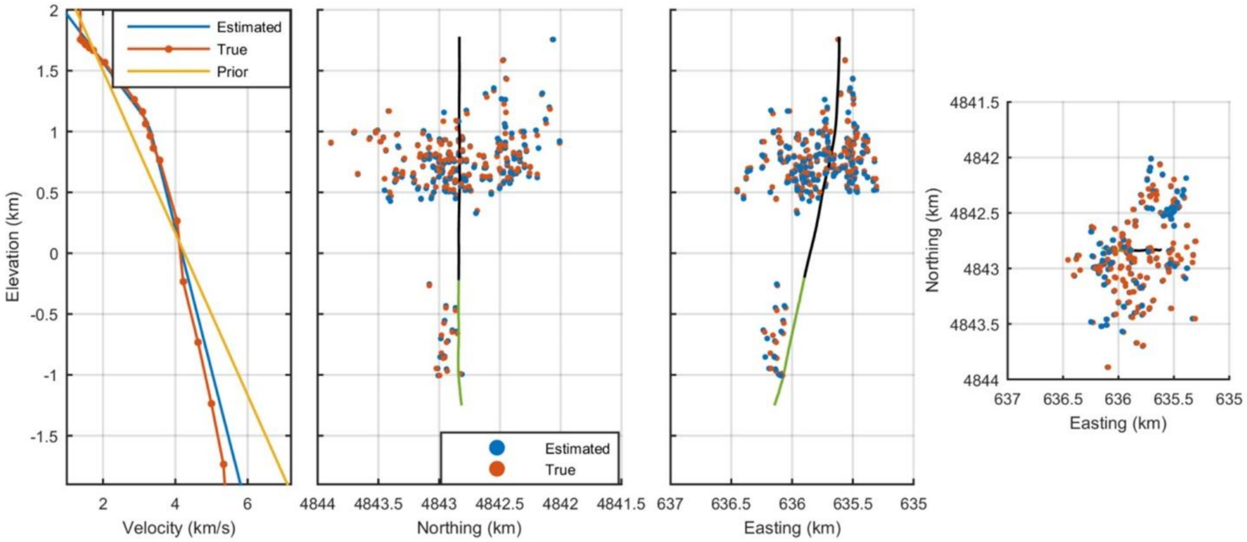

Figure 3-7: The estimated two-layer velocity model can capture the trend of the true multiple-layer model. It did not introduce significant error to the microseismic event locations. This shows that it is adequate to use a two-layer model in this specific scenario.

The result shows that the estimated velocity model (the blue line in Figure 3-7) captures the multiple-layer model relatively well. In addition, the standard deviation of data misfit is 0.0034 s for the P-wave and 0.0045 s for the S-wave. This parameter is a representation of theoretical uncertainty covariance matrix $\mathrm{C_T}$.

It is relatively small compared with observation error C_d in this kind of survey design. As such, it is reasonable to use a two-layer model instead of a multiple-layer model for the simultaneous inversion problem. Additionally, the theoretical uncertainty covariance matrix C_T introduced by the simplification from a multiple-layer velocity model to a two-layer velocity model is not significant.

Admittedly, the ideal earth model is a 3D model. The parameterization error studied in this section is introduced by the simplification from a multiple-layer 1D model. The actual parameterization error can be larger. Estimating a 3D model with adequate regularization is also possible to reduce parameterization error and deserves further investigation.

3.3 Field data

Finally, we applied the simultaneous inversion algorithm to the field data. Figure 3-8 shows our location result along with the result processed by the contractor. Both of the results show two event clusters: the shallow events above 0 km elevation and the deep events near the open-hole portion of the well. The target zone of the stimulation is the formation at the depth of the open hole. However, we see many more microseismic events in the shallow area. After investigation, a borehole television survey found that it is a result of fluid loss from a cracked casing.

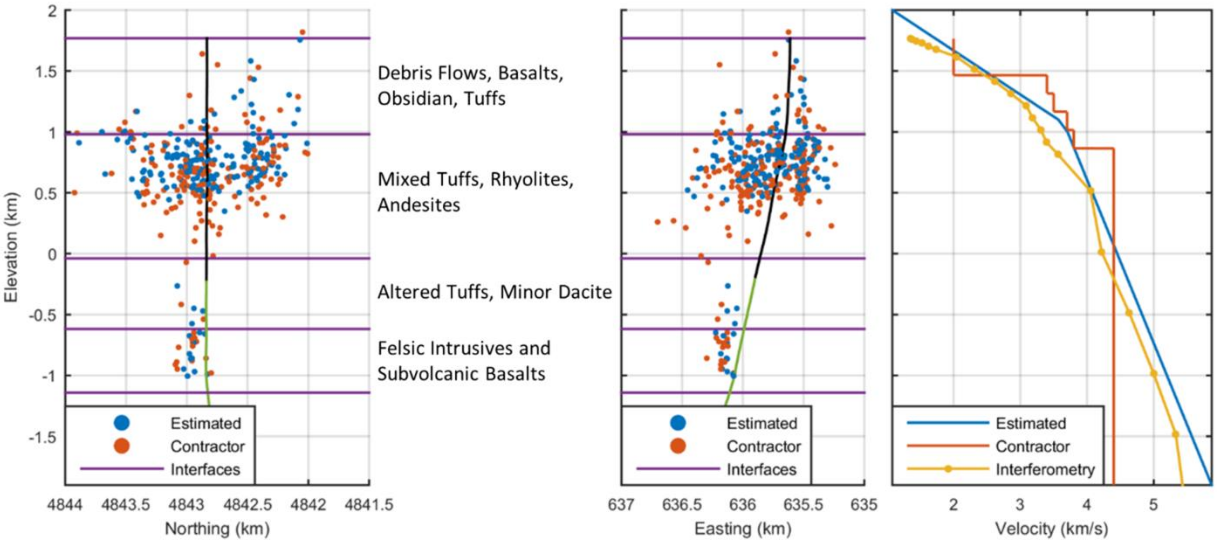

Figure 3-8: Comparison between our simultaneous location result and that provided by the contractor. The simultaneous location result is more clustered than the contractor's result. There is a significant difference in the lower boundaries of the shallow events for the contractor's result (around the elevation of 0 km) and our simultaneous inversion (around the elevation of 0.5 km) due to the difference in the velocity model. The simultaneously inverted P-wave velocity model is very close to the model obtained by seismic interferometry compared with the contractor's model.

Although these two results share a similar microseismic distribution pattern, we find that the microseismic event locations provided by the contractor (red dots) are more scattered than those estimated by our method (blue dots). Another significant difference is that the lower boundary of the shallow events is around the elevation of 0 km, whereas that of the simultaneous inversion is approximately 0.5 km. The histogram of the differences between these two results (simultaneous inversion locations − the contractor's locations) is shown in Figure 3-9. The distribution of the differences in the easting direction has a negative mean value, whereas that in the northing direction has a mean value around zero. This may be a result of the uneven distribution of the surface and borehole stations in the easting direction. Namely, there are more borehole stations to the west of the stimulation zone than to the east. The distribution of the differences in elevation has a much broader distribution due to the large location uncertainty in the vertical direction. The positive mean value of this distribution is mainly a result of the low Vp/Vs used by the contractor compared with our estimated Vp/Vs as will be further discussed in this section.

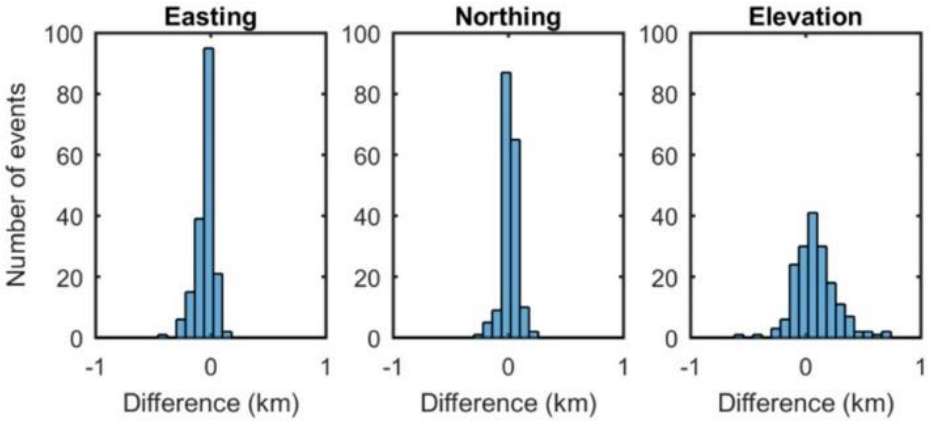

Figure 3-9: The histogram of differences between the MAP estimated result and that provided by the contractor. The histogram in elevation differences has a broader distribution due to the larger location uncertainty in the vertical direction. The positive mean value of this distribution is mainly a result of the low Vp/Vs used by the contractor.

The right of Figure 3-8 is the plot of the velocity models used by the contractor, estimated by our simultaneous inversion using microseismic arrival times, and obtained with seismic interferometry by Matzel, Templeton, Petersson and Goebel (2014). The Vp/Vs value used by the contractor is approximately 1.65, whereas we estimated it to be approximately 1.72. From the comparison of Vp values, we find that the velocity model estimated with our method matches the result of the seismic interferometry relatively well. However, the velocity model used by the contractor is higher than these two results at the elevation interval between 0.5 and 1.5 km. Because the contractor estimated the velocity model with an active-source seismic survey, one possible explanation to the difference between the simultaneous inverted model and the contractor's model is that the raypaths in the active seismic survey can be different from the raypaths in the microseismic survey. With the simultaneous inversion, we were able to construct a velocity model consistent with the raypath coverage of the microseismic survey. To further verify the stability of our simultaneous inversion algorithm for velocity estimation, we randomly divided the 179 microseismic events into two subsets, each of which consists of 90 or 89 events. Then, we estimated the velocity model independently with each of these subsets. The velocity model obtained is shown in Figure 3-10. Although these two velocity models are obtained using two independent microseismic data sets, they match each other very well in terms of VP values as well as Vp/Vs. This demonstrates the stability of the simultaneous inversion for this data set. We may also build velocity models with nonrandom subsets of microseismic events to study the variance over space or time. We have divided the whole 179 events into an east subset (90 events) and a west subset (89 events), as well as a north subset (90 events) and a south subset (89 events). With these subsets of microseismic events, we carried out simultaneous inversion, and the inverted velocity models are shown in Figure 3-11. From this comparison, we can see the Vp and Vp/Vs of the deeper layer are larger for the west and south subsets. This may be a result of the fact that the raypath-covered area is dipping down to the southwest direction (Figure 3-1). Similarly, we may also divide the microseismic events into early and late subsets to study the change of the earth model over time.

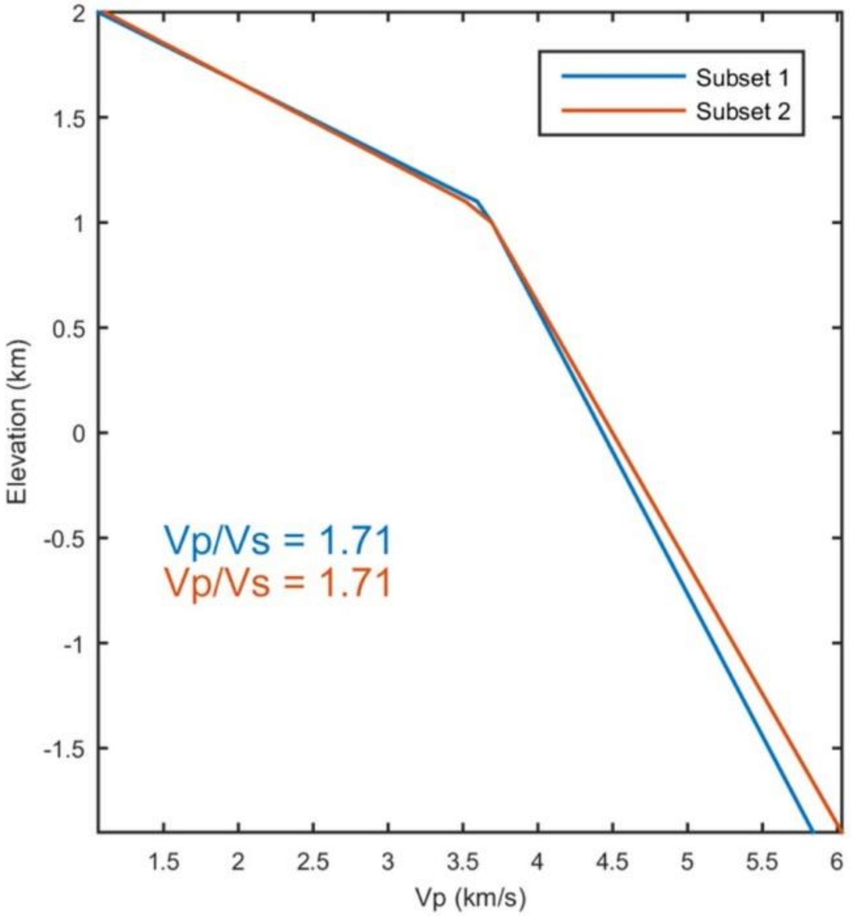

Figure 3-10: Velocity model estimated with two independent subsets of the data. The similarity between these two models verifies the stability of the simultaneous inversion.

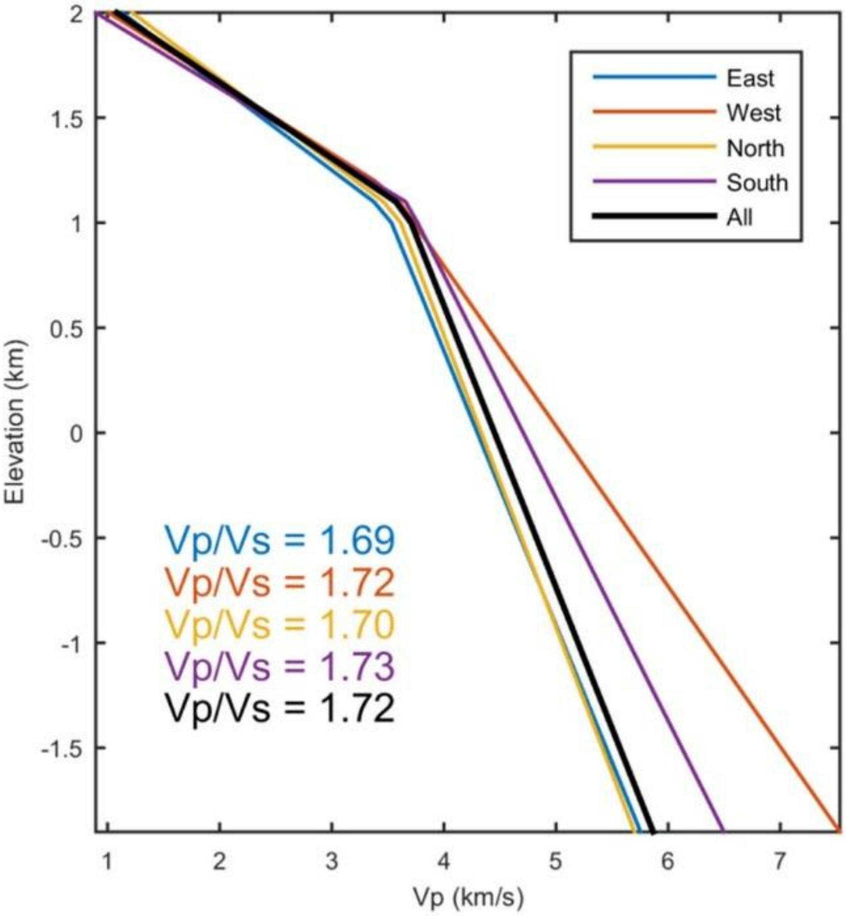

Figure 3-11: Velocity models estimated with microseismic events in various directions. The VP and Vp/Vs of the deeper layer are larger for the west and south event subsets. This may be caused by the dipping of the area downward to the southwest direction (Figure 3-1).

Another advantage of the simultaneous inversion with Bayesian inference is its ability to capture the relationship among various model parameters during the inversion (Poliannikov, Prange, Malcolm and Djikpesse, 2013). Figure 3-12 shows the posterior correlation matrix of the locations and occurrence times of a deep event, a shallow event, and the five velocity parameters. From this covariance matrix, we can see a relatively strong positive correlation between the Vp/Vs and event elevations. This means that an event elevation will increase (decrease in depth) as the Vp/Vs value increases. Thus, the higher Vp/Vs ratio in the simultaneous inversion explains why the inverted elevations are systematically larger than those of the contractor's result.

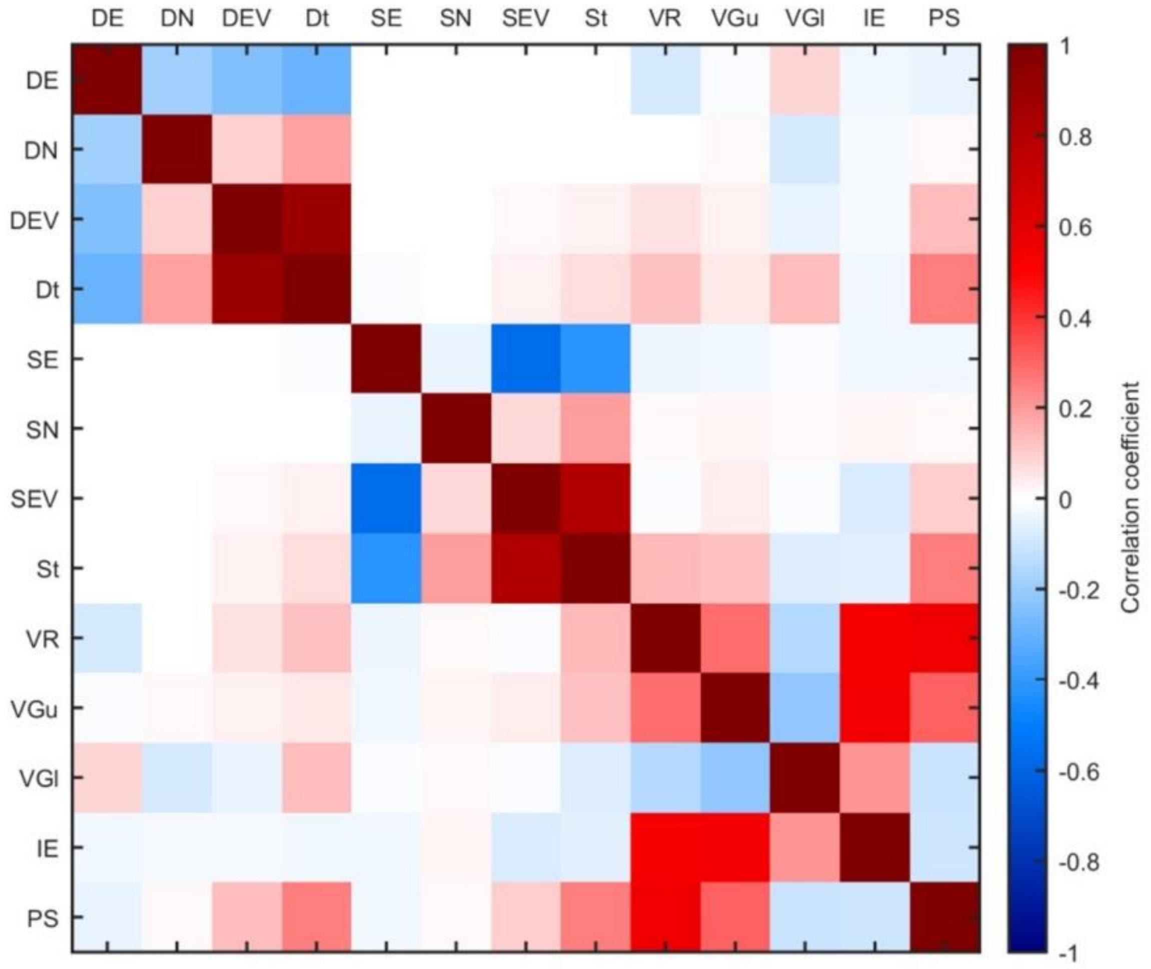

Figure 3-12: Correlation matrix of a deep event, a shallow event, and five velocity parameters. DE, the easting of the deep event; DN, the northing of the deep event; DEV, the elevation of the deep event; Dt, the occurrence time of the deep event; SE, the easting of the shallow event; SN, the northing of the shallow event; SEV, the elevation of the shallow event; St, the occurrence time of the shallow event; VR, velocity at the reference elevation of 1.5 km; VGu, velocity gradient of the upper layer; VGl, velocity gradient of the lower layer; IE, layer interface elevation; and PS, Vp/Vs.

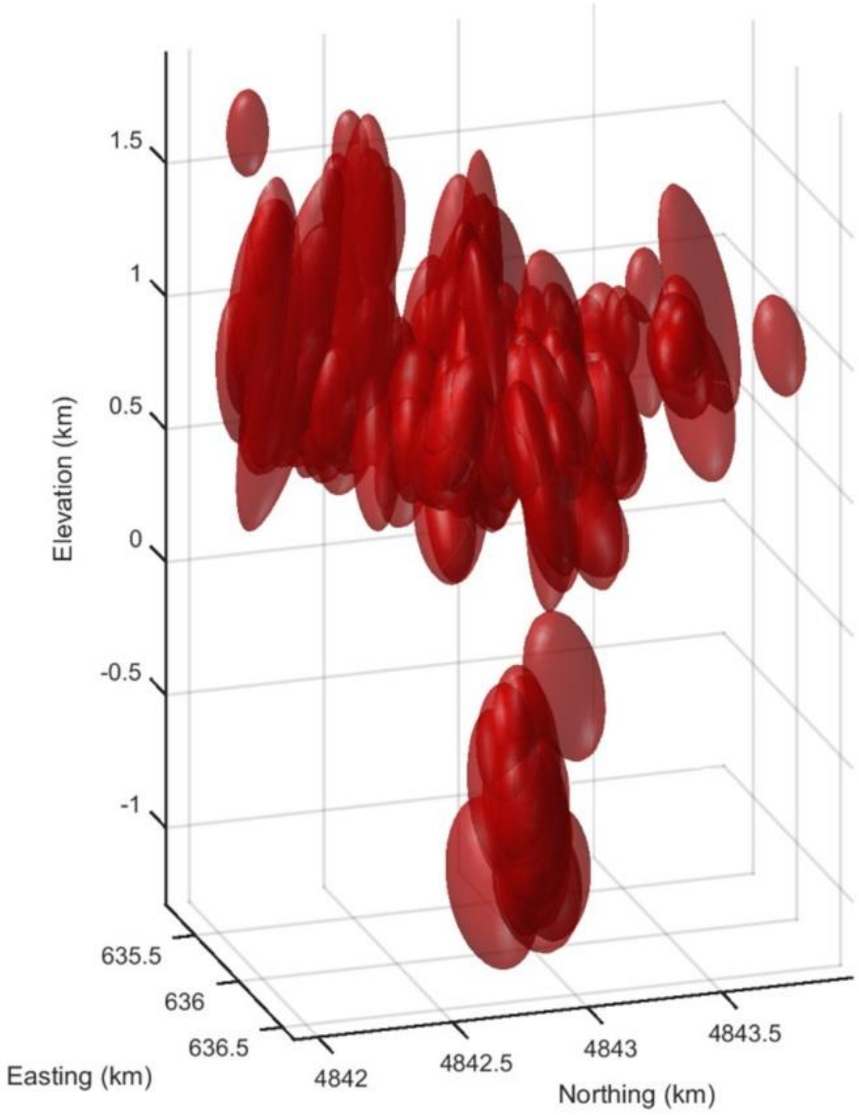

Figure 3-13: The 90% confidence ellipsoids of the estimation of the field data. It shows a similar pattern with the synthetic case. Because the field data include random picking error and the velocity model parameterization error, the size of the confidence ellipsoids is larger than those in the synthetic case.

The 90% confidence ellipsoids of the estimation are shown in Figure 3-13. The error ellipsoids share a similar shape and pattern with those from the synthetic case in Figure 3-5. However, they are larger because the field data includes both random picking error and the velocity model parameterization error.

An example of the improvement in the arrival time match is shown in Figure 3-14. It is a typical event that occurred at the elevation of 0.66 km. The geophone stations are sorted according to the arrival times of the event. Thanks to the simultaneous inversion, the match between the observation and the theoretical prediction has been improved. However, we did not see a systematic change in the arrival-time moveout. This may be due to the irregular geometry of the acquisition or uncertainties resulting from sources other than the velocity model, such as statics.

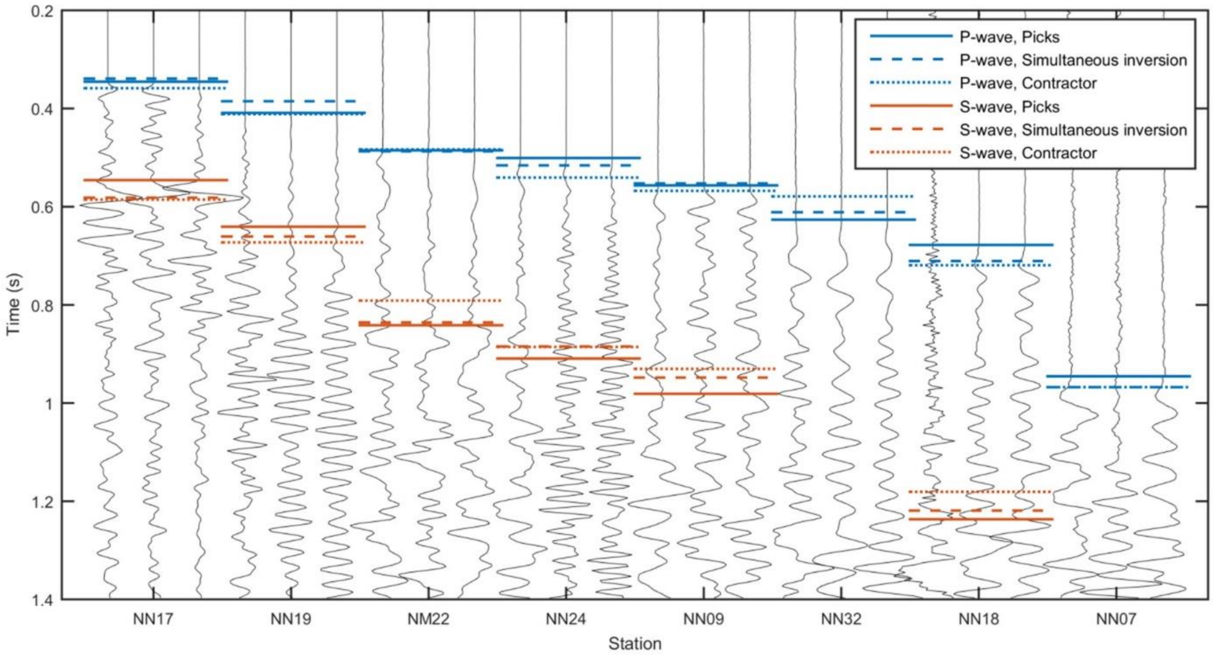

Figure 3-14: Comparison between picks, arrival times predicted by the contractor’s model, and arrival times predicted by simultaneous inversion. Simultaneous inversion was able to improve the match between the theoretical prediction and the real data. However, the improvement is not significant and we did not see a systematic change in the arrival time moveout, probability due to uncertainties resulting from sources other than the velocity model, such as statics.

Figure 3-15 shows the located microseismic events color coded by their occurrence times. From the map view of these events, it is apparent that the early events are mostly near the well, and the late events spread over the entire area. This is because of the time necessary for the propagation of the stimulation fluid to the field far away from the stimulation well.

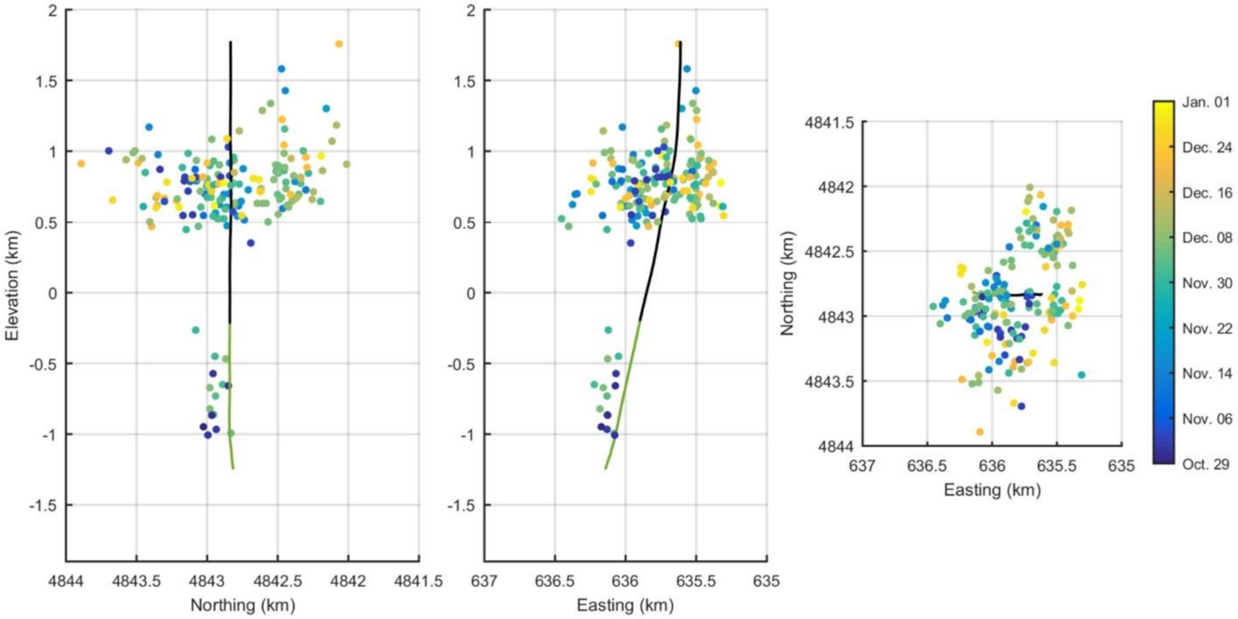

Figure 3-15: Microseismic events color coded by their occurrence times. Early events only occur near the stimulation well. Late events can be either close to or far away from the stimulation well.

Templeton, Johannesson and Myers (2014) compared the well head pressure, flow rate information, and the histogram of the microseismic events as shown in Figure 3-16. There is a good correlation between the well head pressure and the number of microseismic events. The events we are mostly interested in are the small clustered events around the open-hole portion of the well because they are at the target zone.

The black dots in Figure 3-16 show the occurrence times of these deep events. Apparently, they are strongly correlated with the well head pressure. Microseismic events in the target zone only occur when the well head pressure is above approximately 1500 psi due to the fluid loss at the crack as mentioned previously.

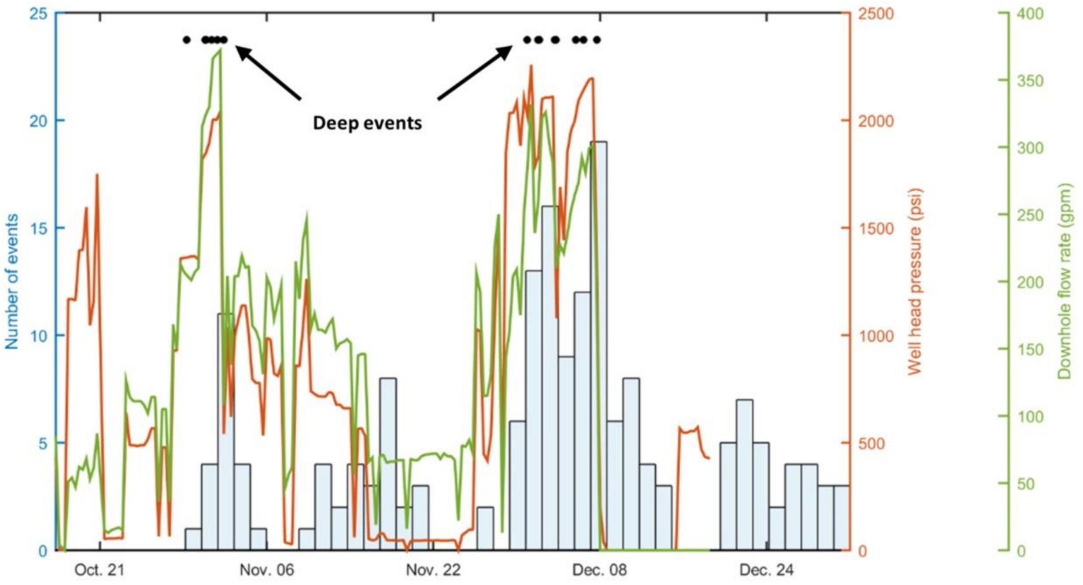

Figure 3-16: Well head pressure, flow rate information, and the histogram (blue bins) of microseismic events. Microseismic events in the target zone only occur when the well head pressure is above approximately 1500 psi.

3.4 Discussion

The MAP point and the covariance matrix approximation of the posterior PDF under a Gaussian assumption are efficient but have some limitations. For example, they may encounter a local minimum problem in the optimization process. The non-Gaussian information and nonlinearity of the problem may also result in a significant bias of this estimation. In these cases, a more sophisticated solution, such as MCMC to the posterior probability density, should be used.

Double-difference earthquake location shows that theoretical error can be significantly reduced by using traveltime differences between nearby events as observations. This correlation between nearby events can be reflected in the off-diagonal entries of the theoretical uncertainty covariance matrix CT. This may be a more efficient method compared with the double-difference location or double-difference tomography due to its low-dimensional data space. Further study will be necessary to make full use of Bayesian inference.

The parameterization of the velocity model can also be a challenging task. It is a trade-off between the accuracy of a model and the well-posedness of the inverse problem. Parameters sensitive to the observations should be chosen, and those insensitive to the observations should be avoided if possible. With careful parameterization of the velocity model and a proper prior constraint on the model, tomography using microseismic data might be promising.

Grechka and Duchkov (2011) and Grechka, Singh and Das (2011) use singular value decomposition to study the roles various anisotropy parameters play in microseismic inversion. They also study the traveltime fit that one can achieve with various numbers of the most important parameters. A similar process can be used to aid in the parameterization of the velocity model in specific acquisition geometries.

If the prior knowledge of the earth model is poor, then the number of microseismic events should be sufficient to constrain the earth model. This makes the application of the simultaneous inversion challenging for the initial state of the hydraulic stimulation. For cases with a relatively good prior earth model, the Kalman filter might be a promising tool to integrate information during the continuous stimulation process (Kalman, 1960).

3.5 Conclusion

We built the framework for simultaneous inversion of multiple microseismic data for event location and velocity model parameter estimation with Bayesian inference. MAP estimation and the covariance matrix under the Gaussian assumption give an efficient and reasonable approximation to the posterior probability distribution. In addition, Bayesian inference enables the uncertainty to be quantified. The application of the developed location algorithm on a synthetic example and the Newberry EGS data shows that we can successfully construct a velocity model from microseismic data as well as estimate the microseismic event locations. The synthetic study shows that the location uncertainty is typically large in the vertical direction due to the limitation of the acquisition geometry, and the situation is worse as the event goes deeper. Implementation on real microseismic data from the Newberry EGS system shows the possibility of constructing a velocity model purely from microseismic data. With the effective velocity model conforming to the microseismic data, we were able to estimate the microseismic event locations without prior knowledge of the earth model.

CHAPTER 4 MICROSEISMIC EVENT LOCATION IN THE MARCELLUS SHALE

4.1 Summary

We studied microseismic data acquired from a geophone array deployed in the horizontal section of a well drilled in the Marcellus Shale near Susquehanna County, Pennsylvania. The geophone array was deployed via a downhole tractor with no mechanical coupling to the borehole wall. We identified that resonances due to poor geophone to borehole coupling hinder arrival time picking and contaminate the microseismic waveform spectrum. We studied its character and analyzed its effect on microseismic data processing. A piking deconvolution filter has been designed to improve the identification of the multiple arrivals; however, it will not help to improve P-wave polarization estimation that was traditionally used to constrain microseismic event locations. We also identified the existence of prominent head waves in some of the microseismic data. The head waves are refractions from the interface between the Marcellus and the underlying Onondaga Formation. The source locations of microseismic events can be significantly improved by using both the P-, S-wave direct arrival times and the head wave arrival times in place the traditional method of using direct arrival times and P-wave polarizations. The traditional method had substantially greater uncertainty in our data due to the large uncertainty in P-wave polarization direction estimation. Our method was applied to estimate the locations of perforation shots as well as microseismic events. Comparison with traditional location results shows improved location accuracy thanks to head wave arrival times. Based on the improvement, we propose a new acquisition geometry and strategy to improve microseismic event location accuracy and reduce acquisition cost in situations such as the one encountered in our study.

4.2 Introduction

Hydraulic fracturing is the process of injecting fluid at pressure that exceeds the minimal principal stress of a formation to create cracks or fractures. It has been successfully used to increase permeability of unconventional reservoirs and stimulate production of a well, and is one of the key technologies in shale gas revolution (King, 2012). Microseismic monitoring has been widely used for hydraulic fracturing monitoring and characterization since its initial implementation (Eisner and Le Calvez, 2007; Warpinski, 2009; Cipolla et al., 2012; Maxwell, 2014). Microseismic acquisition can use surface (Duncan and Eisner, 2010) or downhole (Maxwell et al., 2010) deployments. Shallow wells (typically below the water table) are also used for situations where downhole monitoring is not applicable or not adequate (Cladouhos, Petty, Nordin, Moore, Grasso, Uddenberg, Swyer, Julian and Foulger, 2013). For downhole microseismic monitoring, it is common to have only one nearby well available for microseismic monitoring (Warpinski, 2009). To assist in overcoming the aperture limitations imposed by the acquisition geometry, three-component geophones are deployed, which makes polarization analysis (Yuan and Li, 2016; Yuan, Stewart and Li, 2016) feasible. Moreover, multiple phase identification (Belayouni, Gesret, Daniel and Noble, 2015; Zhang, Rector and Nava, 2015), and full-waveform inversion (Song and Toksöz, 2011) of microseismic signal are also possible in some environments.

However, the coupling between geophones and the wellbore can be poor (J. Du, personal communication, 2016; J. Rector, personal communication, 2016). The poor coupling may lead to severe resonance in seismic waveform and is common in microseismic survey (J. Du, personal communication, 2016; J. Rector, personal communication, 2016). Gaiser, Fulp, Petermann and Karner (1988) conducted an experiment to study the resonance of geophones in a vertical well used for vertical seismic profile (VSP). In their experiment, a geophone was locked in a vertical borehole with a horizontal locking force to imitate a typical VSP condition. They found the geophone was subject to severe resonance issues in the horizontal (radial) component that is perpendicular to the locking arm when the locking force is low. In the cases where the geophones are deployed in horizontal wells as common in microseismic monitoring, the situation is even worse since the only coupling force between the geophone and borehole is usually the gravitational force of the geophone itself. This, together with the unknown orientation of the downhole geophone, makes the microseismic signal analysis with three-component data extremely challenging. Bandpass filters have been designed and applied in previous research to mitigate the effect of downhole geophone resonance (Nava, Rector and Zhang, 2015); however, this is based on the assumption that the resonance frequency is known and different from microseismic spectrum.

Microseismic surveys with a single monitoring well and with only P- and S-wave arrival times result in event locations with ambiguity due to the limited coverage of acquisition geometry. An additional constraint on event location usually comes from direct P-wave polarization (Dreger, Uhrhammer, Pasyanos, Franck and Romanowicz, 1998; Eisner, Duncan, Heigl and Keller, 2009; Li, Li, Morton, Dohmen, Katahara and Toksöz, 2014). Three-component data are necessary for P-wave polarization direction estimation. The major challenges in using three-component data are the unknown orientation of downhole geophones, poor coupling between geophone and borehole wall, and anisotropic/multiple arrival effects in the P-wave polarization estimation. When there are near horizontal raypaths between treatment and monitor wells, arrivals travelling in high velocity layers can affect the polarization estimation of the direct arrival. Perforation shots can be used for geophone orientation calibration. However, depending on the stimulation design, perforation may not have been conducted or recorded by the geophones. These challenges make the uncertainty in the P-wave polarization estimation relatively large, and is usually a major source of microseismic event location uncertainty (Eisner, Duncan, Heigl and Keller, 2009; Maxwell, 2009).

When the seismic source and receiver are both located at nearly the same depth in low velocity shale, head wave arrivals can often be observed. There are numerous examples in the crosswell (Dong and Toksöz, 1995; Parra, Hackert, Gorody and Korneev, 2002; Parra, Hackert, Xu and Collier, 2006) and microseismic (Maxwell, 2010; Zimmer, 2010; Zimmer, 2011) literature where the head wave arrival is the first arrival. People have realized the possible presence of head wave before direct arrival. However, due to its weakness, it has been commonly regarded as contamination of the direct arrival. Synthetic study on making use of head waves has been conducted (Zimmer, 2010; Zimmer, 2011), however, there are few studies using field data on the improvement in event location obtained by using available head waves. Our analysis on microseismic data acquired in the Marcellus shale shows that head waves convey useful information, and can be used to constrain microseismic event location as a substitution for the P-wave polarization.

In this chapter, we first give an overview of the microseismic survey in the Marcellus shale. Then, we present and analyze the resonance in the microseismic waveform acquired in the downhole survey. After that, we study the head waves observed in the Marcellus shale and used them to constrain microseismic event location as a substitution for direct P-wave polarization. Finally, we propose a new acquisition geometry to improve the traditional microseismic acquisition practice based on the location accuracy improvement brought by head wave arrival times.

4.3 Hydraulic fracturing project overview

The hydraulic fracturing project was carried out in the Marcellus formation in Susquehanna County, Pennsylvania, within the Susquehanna River Basin. The Marcellus formation is a Middle Devonian age unit of marine sedimentary shale that contains largely untapped natural gas reserves. It underlies the Mahantango Formation (siltstone and shale) and overlies the Onondaga Formation (limestones and dolostones). Its natural gas trend is the largest source of natural gas in the United States. The Marcellus shale in the studied area has a thickness of roughly 46 m (150 ft) and the average porosity and permeability are respectively 0.08 and 600 nanodarcy.

A multiple well pad that includes seven nearly parallel horizontal wells is the site of field acquisition (Ciezobka and Salehi, 2013). The trajectories of the well laterals are normal to the maximum in situ horizontal stress orientation. The horizontal portions of the wellbores have a spacing of approximately 152 m (500 ft) and an average horizontal wellbore length of 1109 m (3640 ft). The true vertical depths (TVDs) of the wells are approximately 1981 m (6500 ft). The target zone of the wells lies along the lower portion of the Marcellus shale. One of the major purposes of the hydraulic fracturing project was to evaluate the potential to increase stimulation efficiency (increased production, reduced water consumption per unit of gas produced, and reduced environmental footprint) by changing the pump rate. Microseismic data has been acquired and analyzed. Surface microseismic tools were deployed in an approximately 7.8 km^2 (3 square miles) area and 93 stimulation stages were monitored. Downhole geophones were placed in one of the horizontal wells and 62 stimulation stages were monitored. Previous study observed increased microseismicity during hydraulic fracturing in stages with frequency pump rate changes, which suggests better stimulation efficiency (Ciezobka et al., 2016).

Our study is focused on two wells, a monitor well and a stimulation well, as shown by Figure 4-1. The lengths of the horizontal portion of the two wells are 1.35 and 1.7 km, respectively. And the average distance between the horizontal portions of the two wells is around 0.22 km. The stimulation started from the toe and goes until the heel of stimulation well. It consists of 18 stages with an interval of 91 m (300 ft). Each stimulation stage consists 4 perforation shots with a perforation interval of 21 m (70 ft). Eighteen hydraulic fracturing stages were sequentially carried out with four perforation shots prior to each stimulation stage (Figure 4-2). Among these stages, nine were designed to have variable pump rate and nine used the traditional constant rate design. The fracture stages alternated along the horizontal wellbore to account for changes in the reservoir and natural fractures.

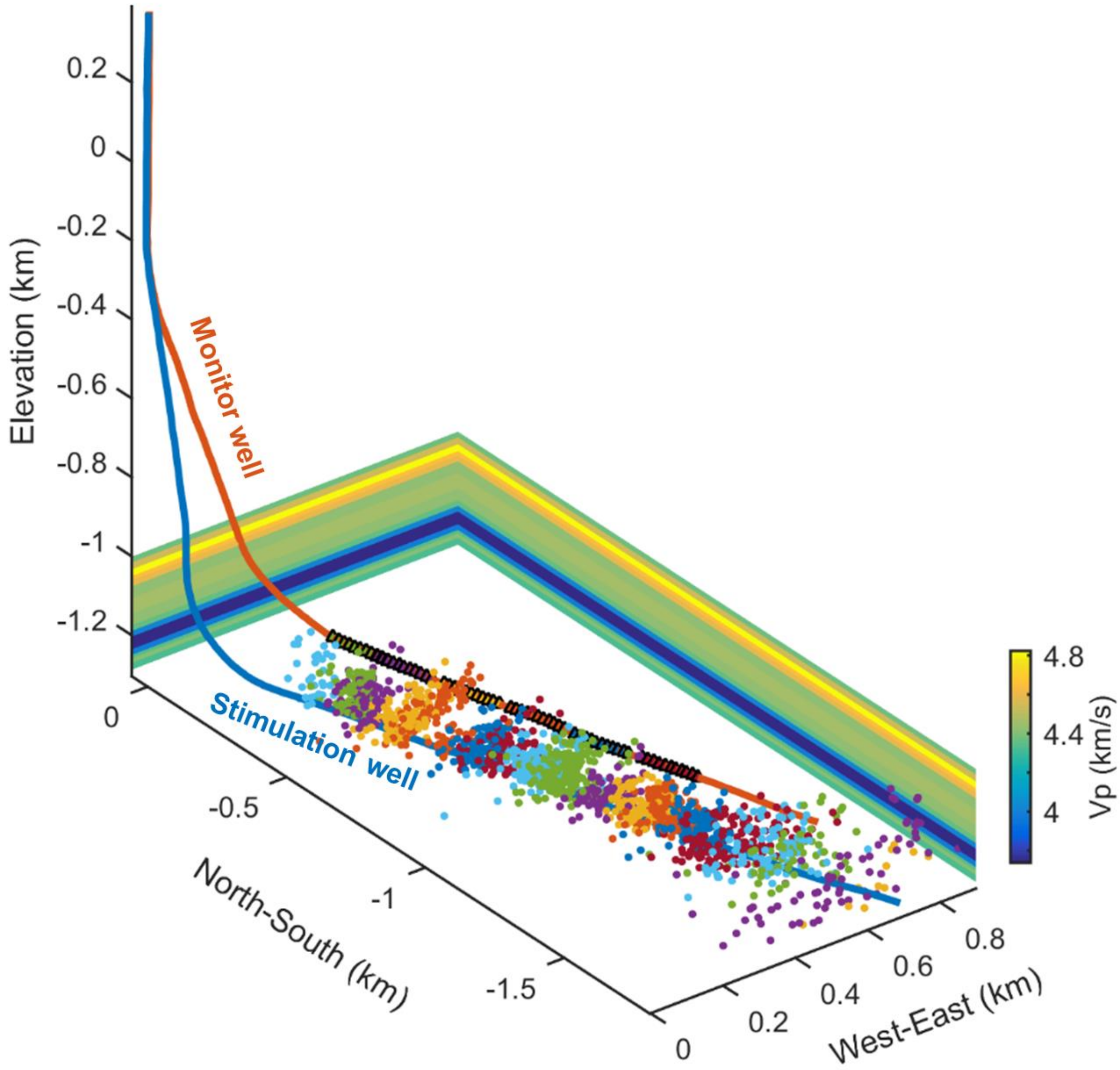

Figure 4-1: Microseismic survey geometry. The microseismic event locations (dots) were located conventionally using P-, S-wave arrival times and P-wave polarization directions. The geophone array is color-coded according to their

locations. Microseismic events are color-coded according to their associated stimulation stages.

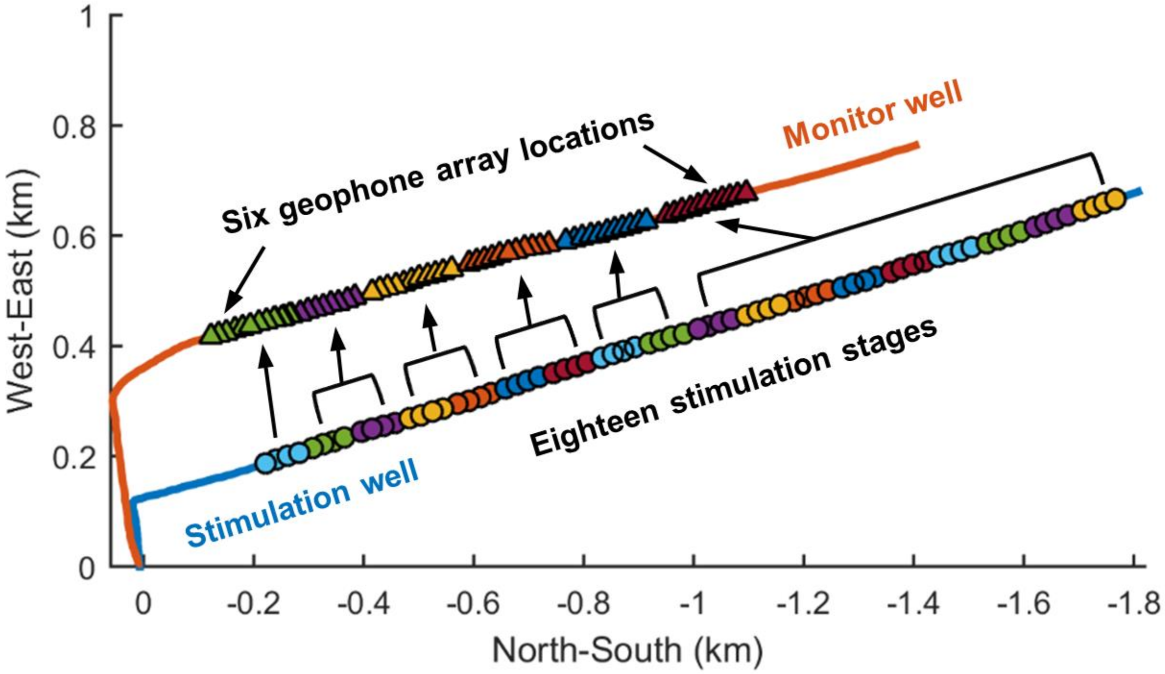

Figure 4-2: Map view of the acquisition geometry. The stimulation was performed in 18 stages and the microseismic signal was recorded by an array of 11 geophones in the nearby monitoring well. The geophone array was moved according to the stimulation stage location to reduce errors due to large event to receiver distances.

The microseismic survey was conducted with an array of eleven three-component 10 Hz geophone tools. The tool spacing in the array was 15.2 m (50 ft). The tools were deployed via tractor in the horizontal section of the borehole and the only coupling between the tool and the borehole wall was due to gravity. As is typical in these types of surveys the tool array was moved along the monitor well bore to be roughly across from the stimulated zone in the treatment well, thereby reducing travel paths length to improve S/N and event location accuracy.

A total of 1842 events were detected and processed during the eighteen stimulation stages. The number of events in each stage is shown in Table 4-1. In addition to these microseismic events, perforation shots from stage 2, 6-9, 12-14, and 17-18 were recorded by the geophone array and used for velocity model calibration and location uncertainty analysis. An isotropic 1D velocity model was created based on a sonic log from the vertical section of the stimulation well and then calibrated with perforation shots as shown in Figure 4-1. The geophone orientations were estimated using the P-wave polarization directions from the perforation shots. P-, S-wave arrival times were manually picked and used for the initial microseismic event location. P-wave polarization directions were also used to constrain microseismic event locations. The microseismic event locations obtained from this analysis are shown in Figure 4-1 and color-coded with their corresponding stimulation stages.

Table 4-1: Number of microseismic events in each stage.

Stage	Number of events	Stage	Number of events
1	11	10	224
2	66	11	168
3	63	12	94
4	93	13	141
5	130	14	101
6	106	15	120

7	141	16	80
8	120	17	70
9	80	18	34

4.4 Data analysis

Figure 4-3 and Figure 4-4 show typical perforation shots (the second perforation shot) and microseismic event waveforms from stimulation stage 6. Examination of the microseismic waveforms acquired in this survey shows frequency resonance in both the axial and radial components of the data. The perforation shot data is also affected by channel dependent resonances. By visual inspection, it can be seen that the characteristic of the resonance is dependent on the channel instead of the source mechanism. The recorded noise-free seismogram due to a microseismic event or perforation shot can be expressed as the convolution of source wavelet, earth impulse response, and geophone response (including resonance due to poor coupling):

$$x(t) = w(t) * e(t) * r(t), \tag{4.1}$$

where $x(t)$ is the recorded seismogram, $w(t)$ is the source wavelet, $e(t)$ is the earth impulse response, and $r(t)$ is the receiver (geophone) response.

Its equivalent form in the frequency domain is

$$X(\omega) = W(\omega)E(\omega)R(\omega), \tag{4.2}$$

where $X(\omega)$, $W(\omega)$, $E(\omega)$, and $R(\omega)$ are the frequency domain representation of $x(t)$, $w(t)$, $e(t)$, and $r(t)$, respectively.

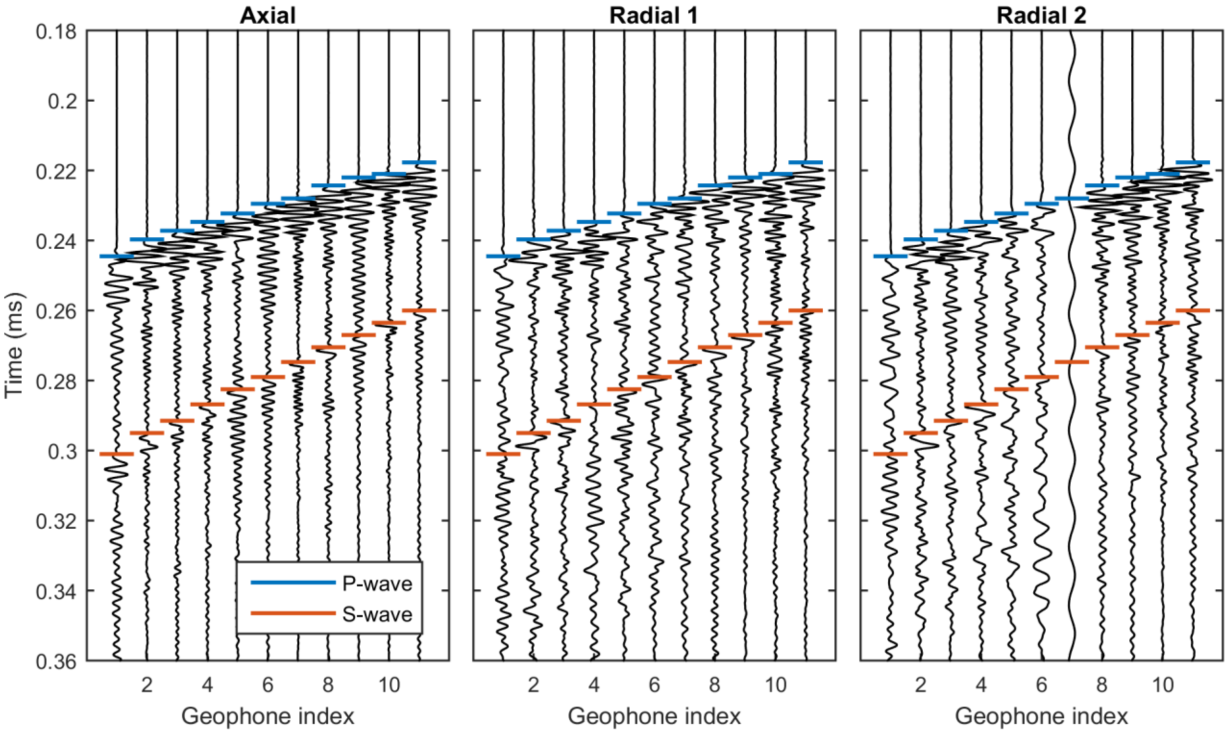

Figure 4-3: Waveforms of a typical perforation shot from stimulation stage 6. The source receiver distance is 0.31 km for geophone 1 and 0.22 km for geophone 11. The waveforms of a perforation shot are usually P-wave dominated due to the source mechanism of perforation shots. Severe resonance effect in waveforms can be observed, especially in the axial component (component 1).

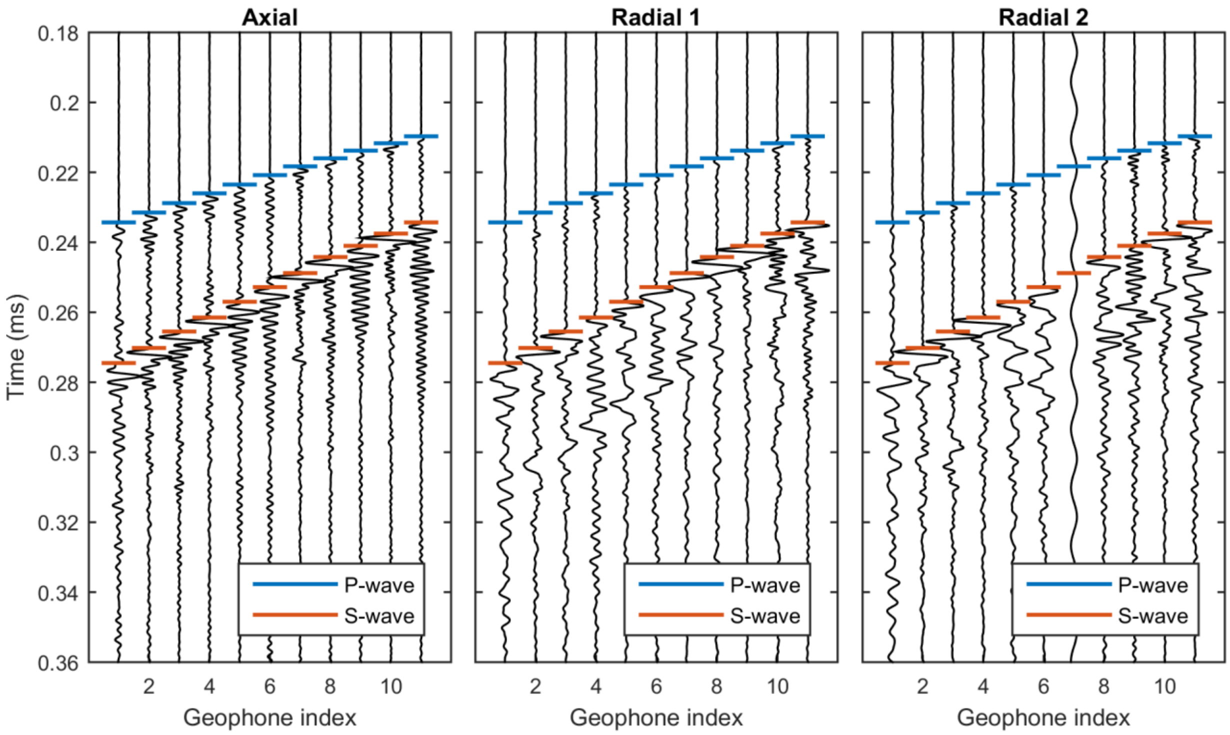

Figure 4-4: Waveforms of a typical microseismic event from stimulation stage 6. The source receiver distance is 0.28 km for geophone 1 and 0.17 km for geophone 11. The waveforms of a microseismic event are usually S-wave dominated.

4.4.1 Spectrum of the resonance

The spectrum of the resonance can be seen from a short-time Fourier transform (STFT) of the three components waveforms recorded by geophone 5 as shown by Figure 4-5. For the axial component, the resonance frequency is around 420 Hz. The first radial component has resonance frequencies of 120 Hz and 440 Hz. The second radial component resonates at 120 Hz and 340 Hz. Gaiser, Fulp, Petermann and Karner (1988)’s experiment shows that the resonance due to poor geophone borehole coupling is mainly on the radial component instead of the axial component. This is the character of the resonance at the frequency around 120 Hz. The fact that the only coupling force between the geophone and the wellbore in the horizontal well should be the reason for the resonance in both radial components. The resonant frequencies of a geophone due to poor geophone-borehole coupling are dependent on the mass of the geophone, the contact surface geometry, borehole geometry, locking force, etc. (Gaiser, Fulp, Petermann and Karner, 1988). The resonance around 400 Hz may result from the resonance of the geophone themselves. Resonance will create problems for such things as Q value estimation, waveform inversion, and P-wave polarization direction estimation. In the presence of resonance, additional processing procedures should be taken such as the relative spectrum analysis introduced by Zhang et al. (2016).

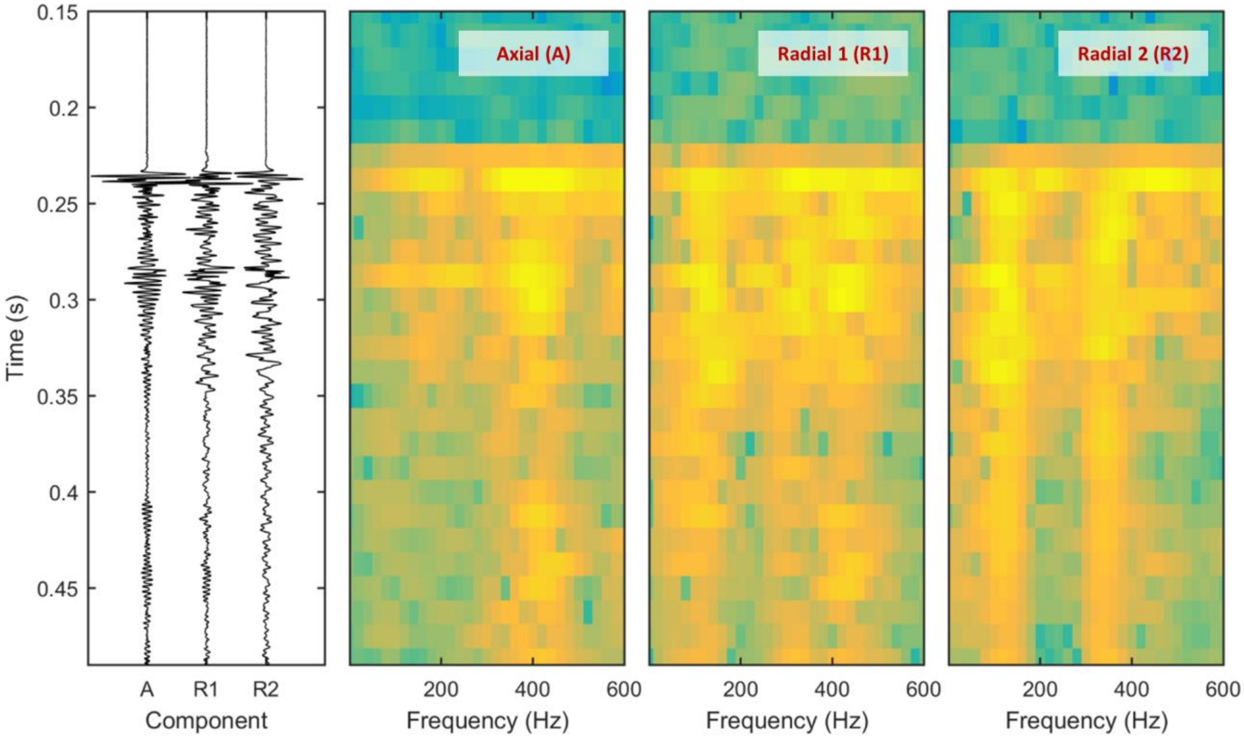

Figure 4-5: STFT of a typical three-component waveform generated by a perforation shot. For the axial component, the resonance frequency is around 420 Hz. The first radial component has resonance frequencies of 120 Hz and 440 Hz. And the second radial component resonates at 120 Hz and 340 Hz. The resonance around 120 Hz maybe be due the poor coupling between geophone and wellbohre. And the resonance around 400 Hz may result from the resonance of the geophone themselves.

4.4.2 Deconvolution of microseismic signal

The presence of resonances in microseismic signals may affect the identification of seismic phases. The effects of receiver resonances in the receiver signature can be attenuated with receiver channel consistent deconvolution (Claerbout, 1992; Yilmaz, 2001). The deconvolution improves the compactness of the microseismic wavelet and can help in the identification of seismic phases by recovering the impulse response of the earth. Under the assumption that the impulse response of the earth, $e(t)$, is random ($|E(\omega)|$ is constant in the frequency domain), the seismogram has the same amplitude spectrum, $|X(\omega)|$, with the amplitude of the convolution of the source wavelet and the geophone response, $|W(\omega)R(\omega)|$. An additional minimum phase assumption enables the determination of an optimum Wiener filter, which can recover the impulse response of the earth from the recorded seismogram (Yilmaz, 2001). This can be used to remove the geophone resonance, thus, improve the identification of the multiple arrivals.

We performed a spiking deconvolution to remove the receiver signatures in these waveforms. The optimum Wiener filter was designed using the average autocorrelation of the four perforation shots in stage 6. The waveforms before and after deconvolution are shown in Figure 4-6. From the comparison, we can see a significant suppression of the resonance following the P- and S-wave arrivals after the deconvolution. This suppression prevents the later phases from being contaminated by resonance due to earlier arrivals. For instance, it can be difficult to determine the S-wave arrival times on geophone 5 and 9 in Figure 4-6 due to their preceding resonance. However, after the removal of the resonance, it is significantly easier to pick those arrivals. In addition, we also find two weak, yet clear phases after the deconvolution denoted by multiple 1 and multiple 2 in Figure 4-6. These two arrivals can hardly be identified in the original data.

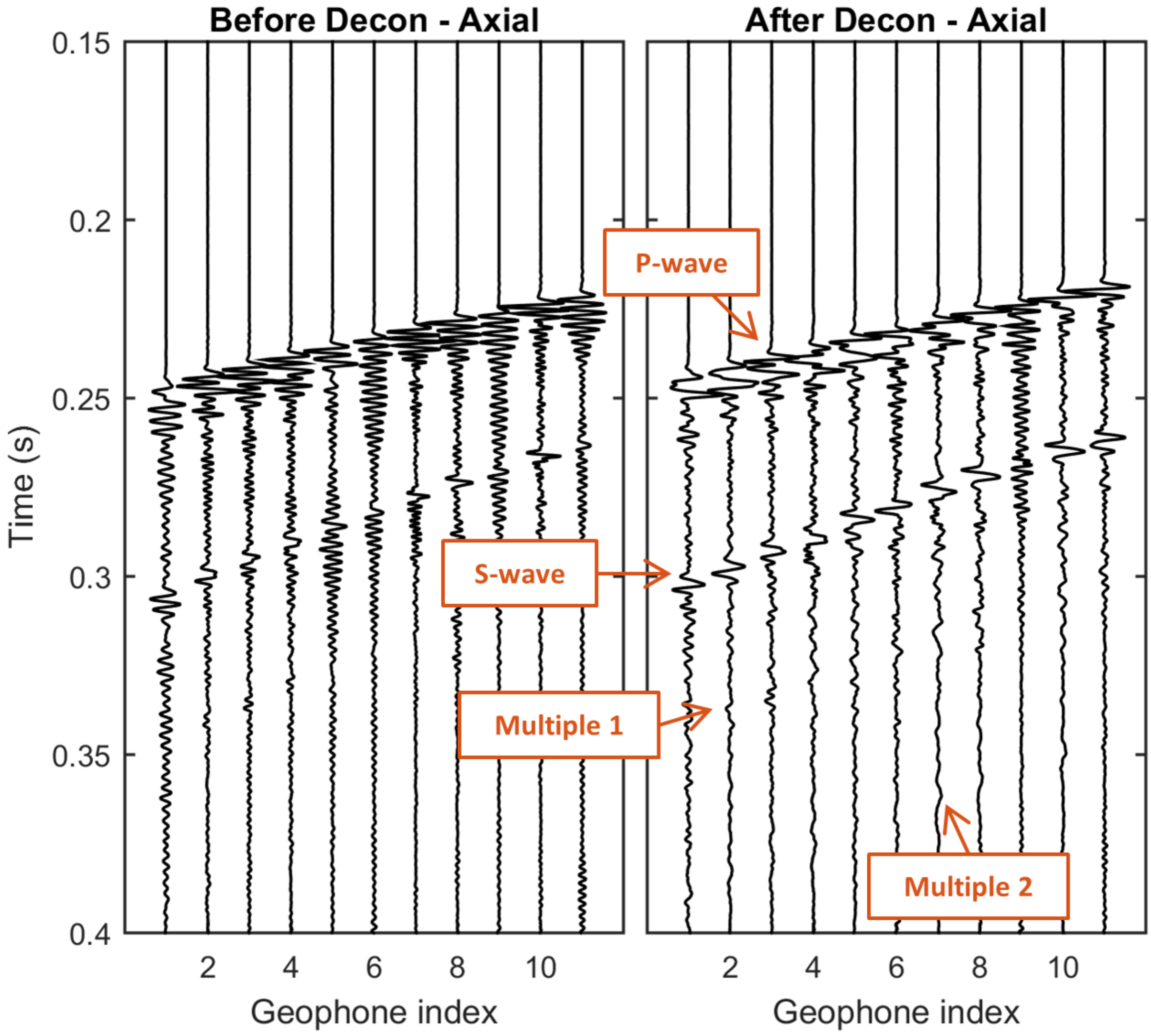

Figure 4-6: Deconvolution result of the axial component. The source receiver distance is 0.31 km for geophone 1 and 0.22 km for geophone 11. The deconvolution successfully suppressed the resonance in the original data. In addition, it enhances multiple arrivals that are hardly identified in the original waveform.

4.4.3 Relative spectrum analysis

From Equation (4.2) For any microseismic event with index i, the ratio between its waveforms in the Fourier domain and the average spectrum over all the N events recorded by the same geophone can be expressed as

$$\frac{X_i(\omega)}{\sum_{n=1}^{N} X_n(\omega)} = \frac{W_i(\omega)E_i(\omega)R(\omega)}{\sum_{n=1}^{N} W_n(\omega)E_n(\omega)R(\omega)} = \frac{W_i(\omega)E_i(\omega)}{\sum_{n=1}^{N} W_n(\omega)E_n(\omega)}. \qquad (4.3)$$

Again, under the assumption that the impulse response of the earth is random, the Fourier representation $E_n(\omega)$ is white. So, the relative spectrum of event i is approximately equal to

$$\frac{X_i(\omega)}{\sum_{n=1}^{N} X_n(\omega)} \approx \frac{W_i(\omega)}{\sum_{n=1}^{N} W_n(\omega)}. \qquad (4.4)$$

This expression is not affected by the receiver response $R(\omega)$, so it is a better representation of the real spectrum of the microseismic event.

Figure 4-7 shows the effect of relative spectrum analysis compared with single waveform spectrum analysis. Figure 4-7a and Figure 4-7b show 52 single microseismic event spectra of P-wave and S-wave. The events are sorted according to the peak frequency of P-wave spectrum. However, we cannot see any effect of this sorting in the S-wave spectrum (Figure 4-7b).

Then, we normalized the P-wave and S-wave spectrum with their average over all these microseismic events. The result is shown in Figure 4-7c and Figure 4-7d. Compared with the spectrum of single events, the relative S-wave spectrum shows a similar trend (Figure 4-7d) with that of P-wave after the events are sorted with peak P-wave spectrum. This shows that there is an intrinsic correlation between P-wave and S-wave spectrum of the same event. The spectrum of single microseismic event does not have this trend due to the effect geophone resonance. The relative spectrum analysis is able to reveal this correlation.

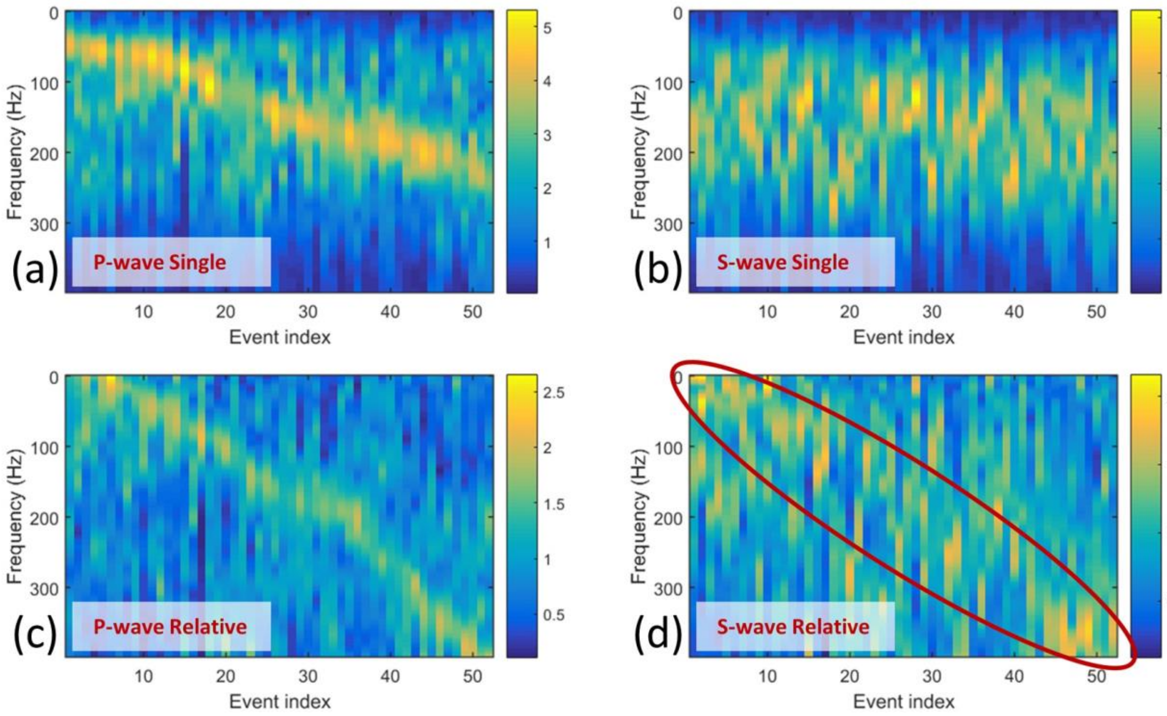

Figure 4-7: Single spectrum analysis (a and b) and relative spectrum analysis (c and d). The events are sorted according to the peak frequency of P-wave spectrum. The relative S-wave spectrum (d) shows a similar trend with P-wave spectrum (c). However, we cannot see this phenomenon from the single spectrum analysis.

4.5 Head wave

Due to the azimuthal ambiguity in microseismic event location using only P- and S-wave arrival times, P-wave polarization is commonly used to constrain the azimuthal direction of microseismic events. However, the effect of resonance on the downhole geophones may result in large uncertainty in P-wave polarization estimation. In addition, the orientations of downhole geophones will require calibration using information from perforation shots, which may be unavailable. Due to the low velocity nature of shale, the head wave is commonly identified in microseismic surveys (Maxwell, 2010; Zimmer, 2010; Zimmer, 2011). Like other microseismic surveys, we observed head waves in the Marcellus shale. In this section, we use the head wave arrival times as a substitution for the P-wave polarization to constrain the microseismic event locations.

4.5.1 Head waves

Figure 4-8 shows the axial component of the waveforms for perforation shot 4 in stage 2. The head wave arrivals have low amplitude and high velocity moveout as annotated by the yellow picks in Figure 4-8. The generation mechanism of head waves in the Marcellus can be seen from Figure 4-9, which is a common acquisition configuration in shales. If the velocity of a nearby layer (the Onondaga Formation in this case) is larger than the shale, and assuming both source and receiver are located in the shale, head waves will be generated when the angle of incidence is equal to a critical angle $\arcsin(V_1/V_2)$, where V_1 and V_2 are the velocities of the low and high velocity layer as shown in Figure 4-9. The head wave will then travel along the formation interface until the point where it refracts back to the original low velocity layer with angle of emergence at the critical angle. P-P-P, S-S-S, and S-P-P, and P-P-S converted head waves are potentially identifiable. In practice the three latter head waves are difficult to identify because they occur after the first arrival. Also, a dip-slip microseismic focal mechanism which is often thought to be the dominant rock breaking mechanism (Rutledge and Phillips, 2003) will preferentially generate P-P-P arrivals. The Direct arrival amplitude is inversely proportional to the distance that the seismic ray traveled from the source due to geometrical spreading, while head wave amplitude is approximately inversely proportional to the square of this distance (D. Dreger, personal communication, 2014). Thus, the head wave will decay faster than the direct arrival and usually has smaller amplitude. As in refraction seismology, though the head wave travels a longer path than the direct arrival, it arrives before the direct arrival past the cross-over distance. Figure 4-10 shows traveltime versus source/receiver separation for the configuration in Figure 4-9.

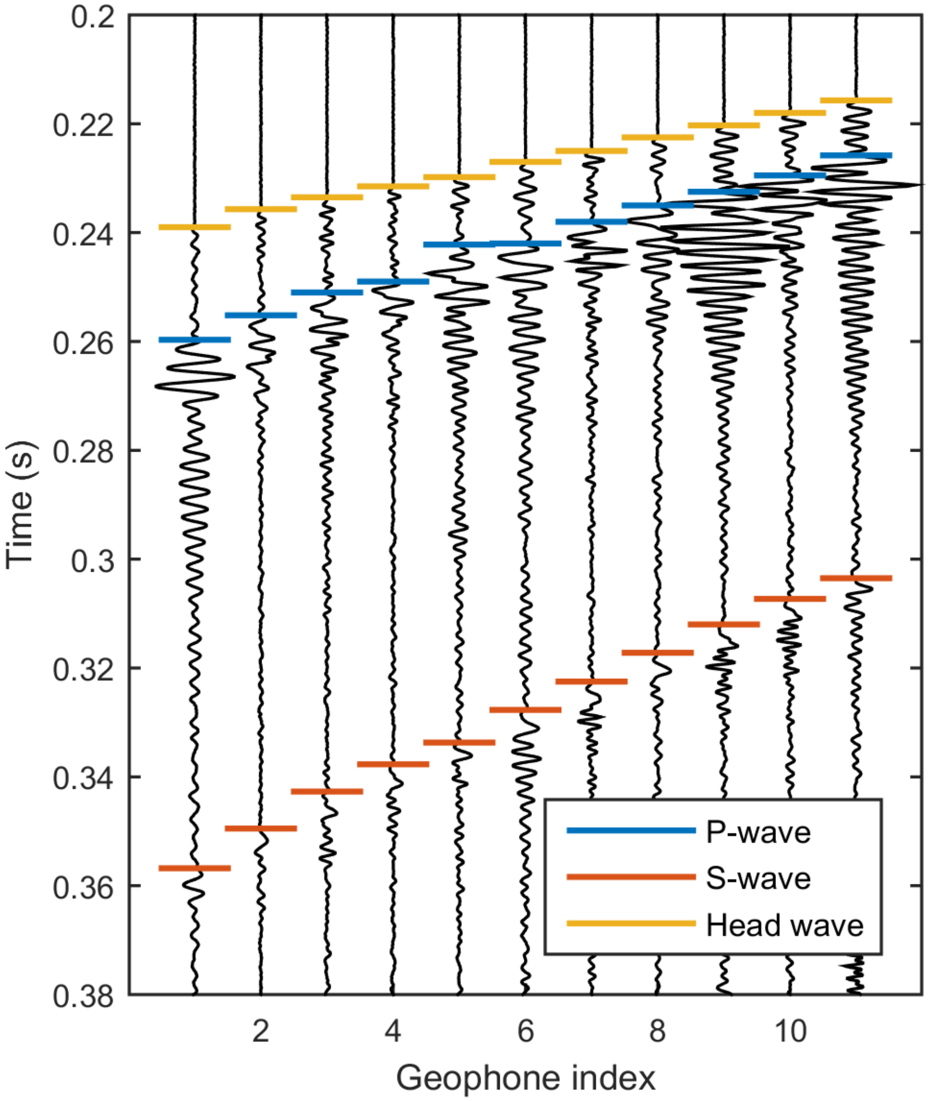

Figure 4-8: The axial component of the waveforms of a perforation shot recorded by an array of geophones. The source receiver distance is 0.67 km for geophone 1 and 0.53 km for geophone 11. Head waves can be easily identified based on their low amplitude and high velocity moveout.

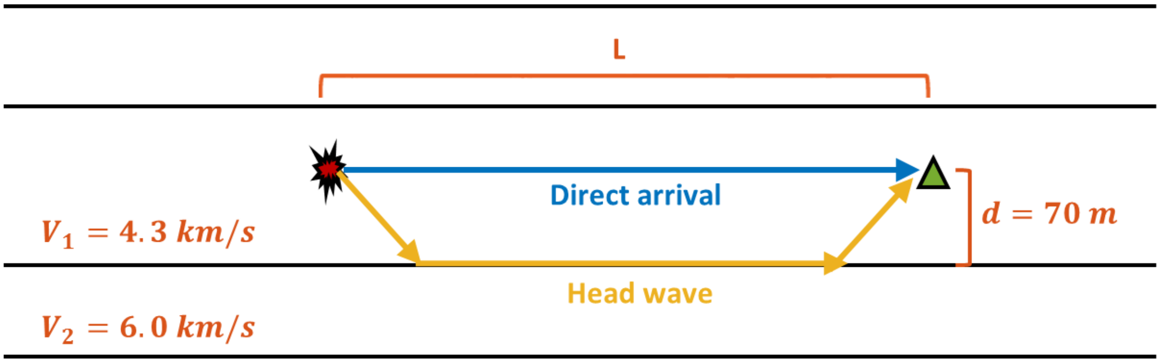

Figure 4-9: A common configuration for a head wave. Due to the low velocity nature of shale, the head wave is commonly identified when there is a nearby high velocity layer.

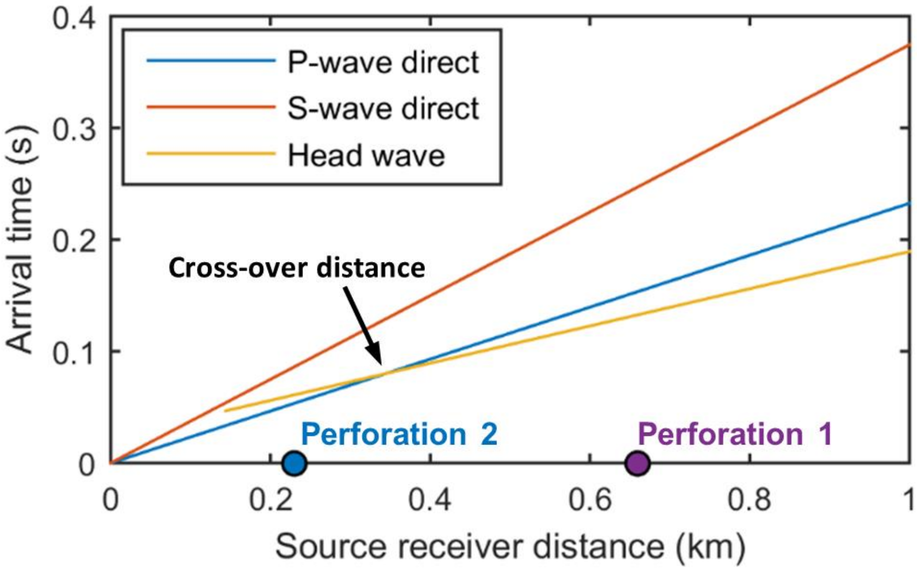

Figure 4-10: Arrival time of various phases as a function of source receiver distance. When source receiver distance is larger than the cross-over distance, the head wave can overtake the direct arrival to be the first arrival. Perforation 1 and Perforation 2 are respectively two perforation shots with source receiver distance larger and smaller than the cross-over distance.

4.5.2 Velocity model calibration

Since the original velocity model is a model based on sonic logs and calibrated with perforation shots, it is limited to the TVD of the kickoff point (sonic logs are not typically run in the horizontal section). The head wave will not take over the direct P-wave to be the first arrival as observed in the waveform within the offset ranges in this study. To calibrate the velocity model, perforation shots were used and P, S, and head wave arrival times were picked (Zhang et al., 2017). From the calibrated velocity model, we found that Marcellus velocities near the stimulated interval were similar to the one provided by the contractor. The calibration also reveals the existence of a high velocity ($V_p = 6.01\ km/s$) formation, Onondaga Formation, underlies approximately 70 m below the geophone array. However, there was no velocity information in the original model due to lack of sonic logs.

4.5.3 Finite difference simulation

To further verify the existence of head waves and the calibrated velocity model, we conducted finite difference simulation to investigate the wave propagation of microseismic signals with a 3D explicit 4th order time and space elastic forward modeling code (Petersson and Sjogreen, 2013). The focal mechanism of the source is assumed to be a vertical crack. The source time function is assumed to be a Ricker wavelet with peak frequency at 100 Hz. The existence of head waves can be verified by the comparison between real and synthetic waveform as shown by Figure 4-11. Both the amplitude and arrival time of head wave in real data match the synthetic waveform relatively well. The differences in the S-wave in the Vx and Vy components may be due to the lack of knowledge of source mechanism of the real event for the finite difference simulation.

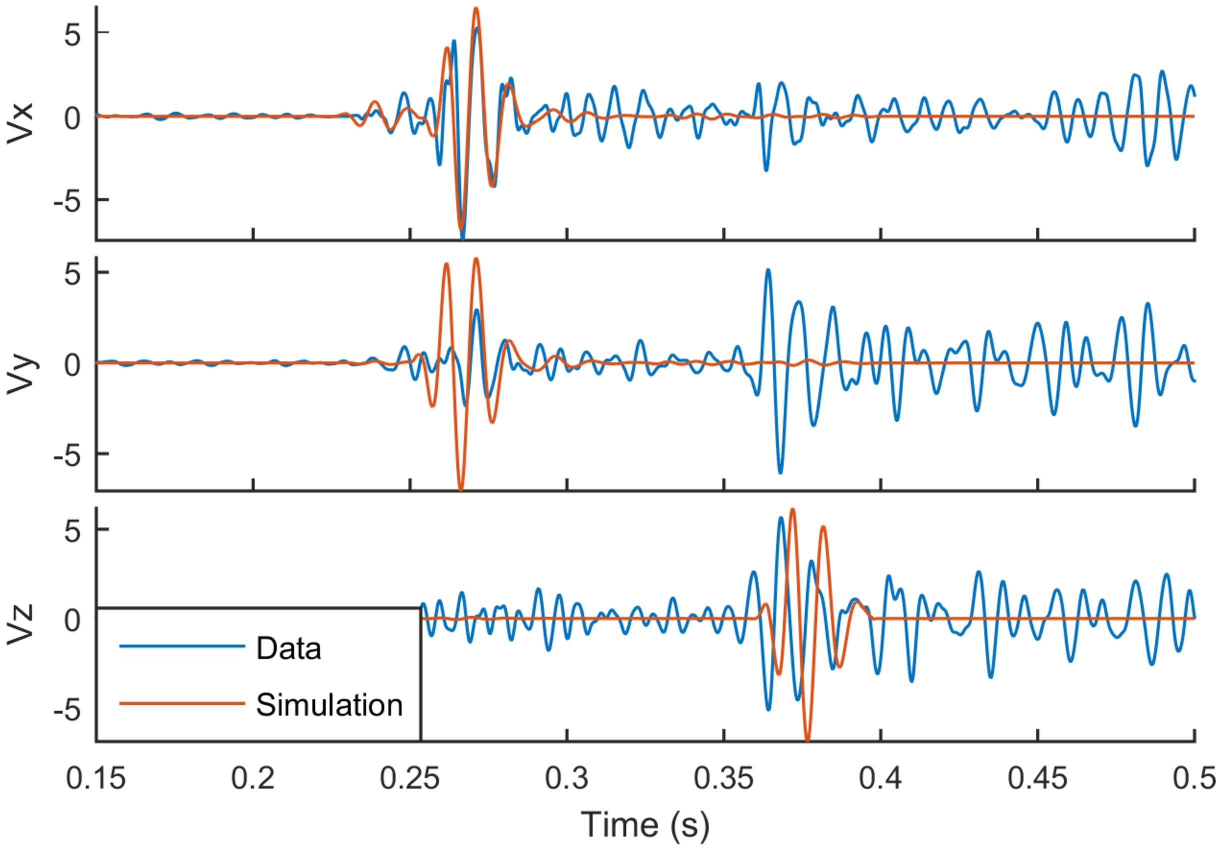

Figure 4-11: Comparison between synthetic and real waveform. The synthetic waveform matches the real data relatively well, which verifies the existence of head wave. The difference between the S-wave in the x and y components may be due to the unknown source mechanism of the real event for simulation.

4.5.4 Perforation shot location

To quantify our event location estimation uncertainty, we located the perforation shots in stage 2 with a Jackknife technique (Miller, 1974). That is, for each perforation shot, its location is estimated with the velocity model calibrated with the other three perforation shots. Since the velocity model was not calibrated with the perforation shot to be located, these perforation shots in stage 2 can be treated as normal microseismic events and used for location uncertainty analysis. Our location result of the four perforation shots along with their true location is shown in Figure 4-12. What is also shown is the location result with the traditional method, which used direct arrivals and P-wave polarization directions.

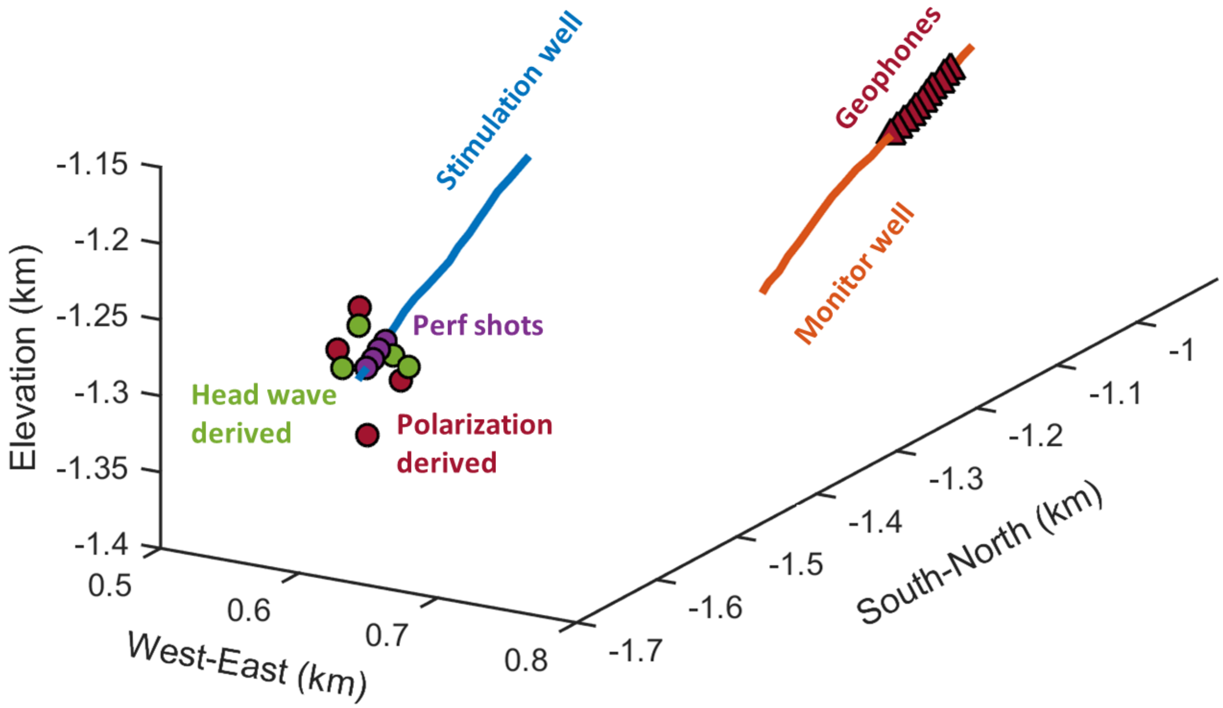

Figure 4-12： Comparison of estimated perforation shot locations and the true perforation locations. The perforation shot locations derived with P-, S-, and head waves is more accurate than the result using P-wave polarization as a constraint.

From the comparison, we found the method using head waves gives a root mean square (RMS) error of 19 m while the traditional method with P-wave polarizations gives a RMS error of 52 m. Given the limited acquisition geometry and relatively large source receiver distance in this survey, the method using head wave arrival times gives improved location accuracy while the traditional method using P-wave polarization directions leads to relatively large uncertainty.

4.5.5 Relocation of events in the second stage

A map view of the microseismic event locations estimated with the traditional P-wave polarization method is shown in Figure 4-13. Note that the microseismic event locations in stage 2 are significantly more scattered than those in later stages. One possible explanation to this scattering is because of the larger stimulated reservoir volume associated with stage 2 stimulation. However, an alternative explanation is simply because of the larger event location uncertainties in stage 2 events due to the longer travel paths.

We relocated these events using direct P, direct S and head wave arrivals without polarization as shown in Figure 4-14. The relocated events are much less scattered than the result estimated with the traditional location method. Also, it indicates the effectiveness of using head wave arrival times in microseismic event locations to improve event location accuracy.

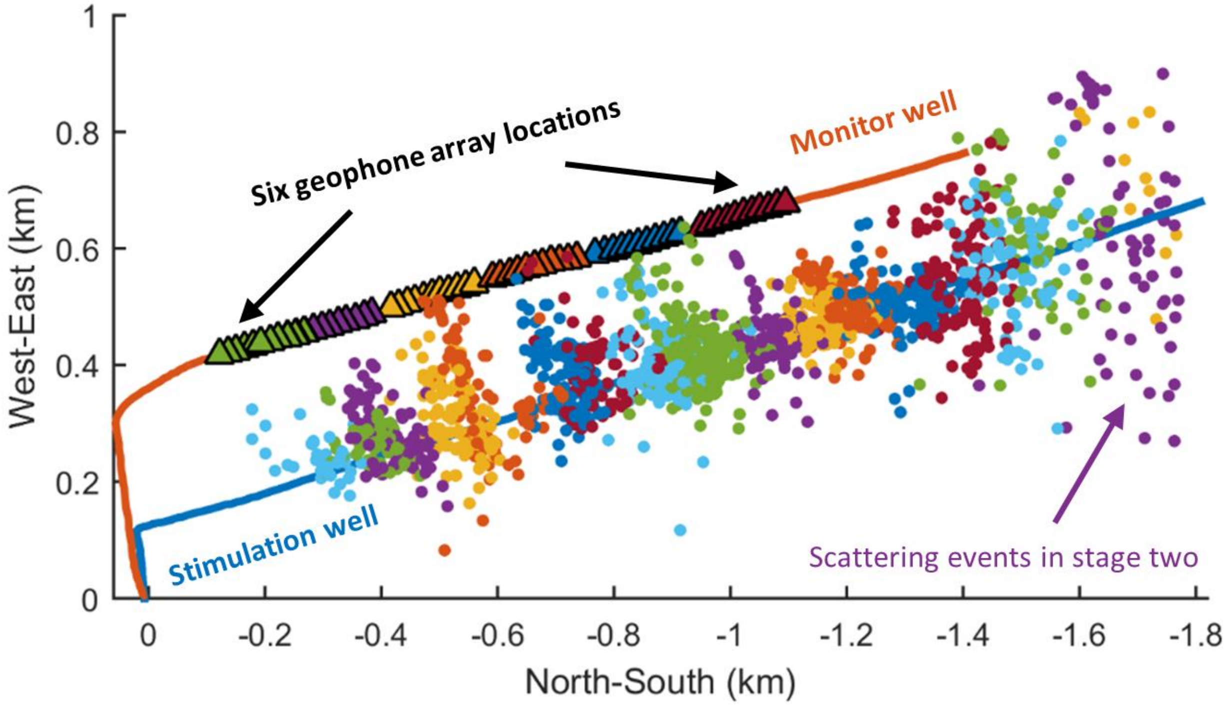

Figure 4-13: Map view of microseismic event locations processed using P-, S-wave arrival times and P-wave polarizations. The event location in stage 2 is much more scattered than those in later stages.

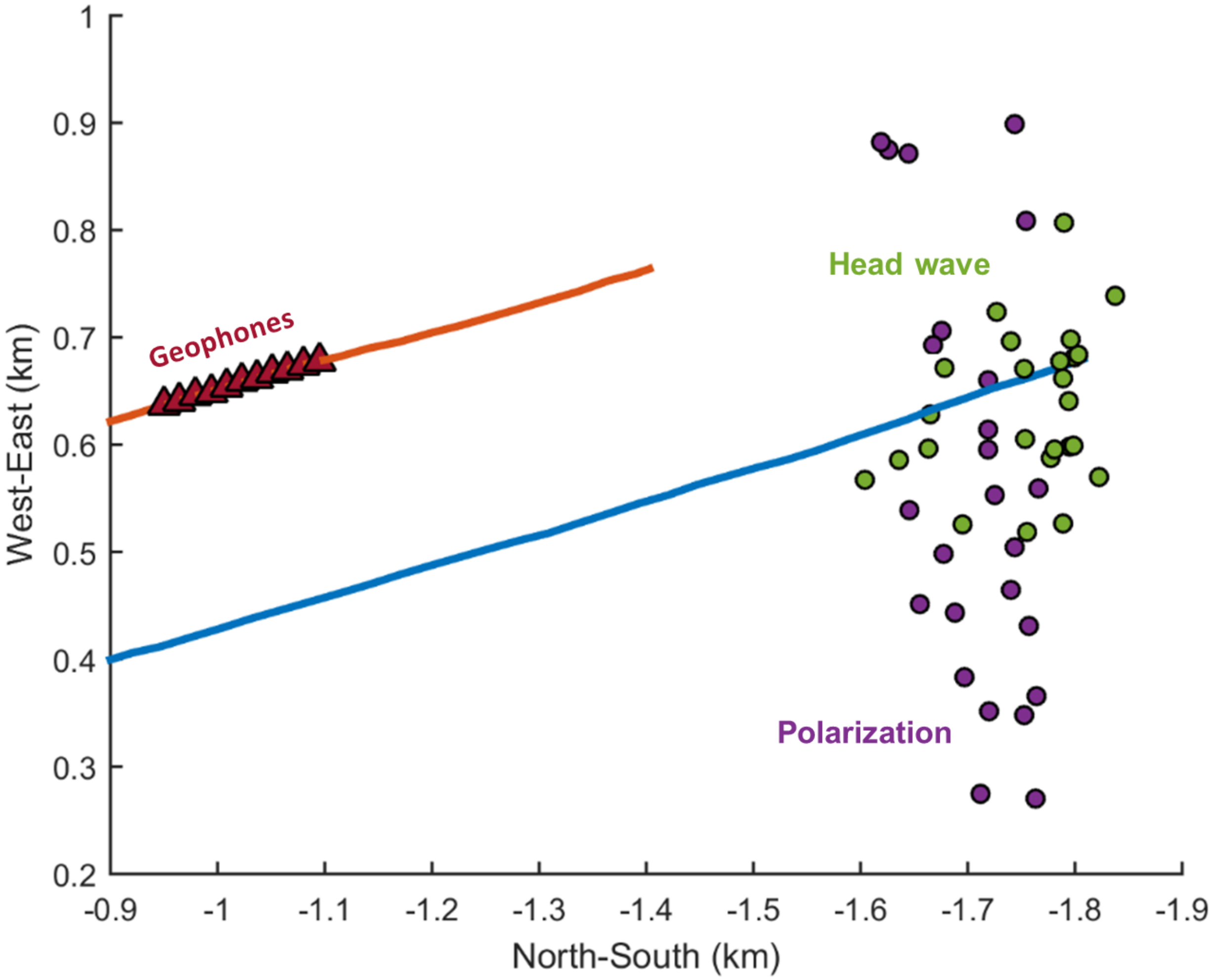

Figure 4-14: The microseismic event locations estimated with P-, S-, and head wave arrival times are less scattered when compared with the microseismic event locations processed using the traditional location method.

4.5.6 Acquisition geometry

In some situations, such as the data from Figure 4-15, the head wave is not the first arrival. When the source receiver distance is smaller than the cross-over distance such as the data in Figure 4-15, which comes from perforation shot 2, head waves will arrive after the direct P-waves (Figure 4-10). In this case, it will be more difficult to pick head wave arrivals, and conventional methods of event location using P-wave polarization directions may be required to constrain the event locations. Traditional acquisition practices place the geophone array as close as possible to the stimulation zone. However, our analysis shows this practice may result in loss of information with multiple arrivals. We would propose to place the geophone array farther than a cross-over distance for single horizontal well monitoring as shown by Figure 4-17. This acquisition geometry will enable the identification of multiple arrivals; thus, improve microseismic event location accuracy. Moreover, fewer moves (perhaps no moves whatsoever) may be required to provide accurate location information. Significant reductions in acquisition cost and wellbore risk might be achieved with this geometry without sacrificing accuracy and in some situations perhaps improved location accuracy.

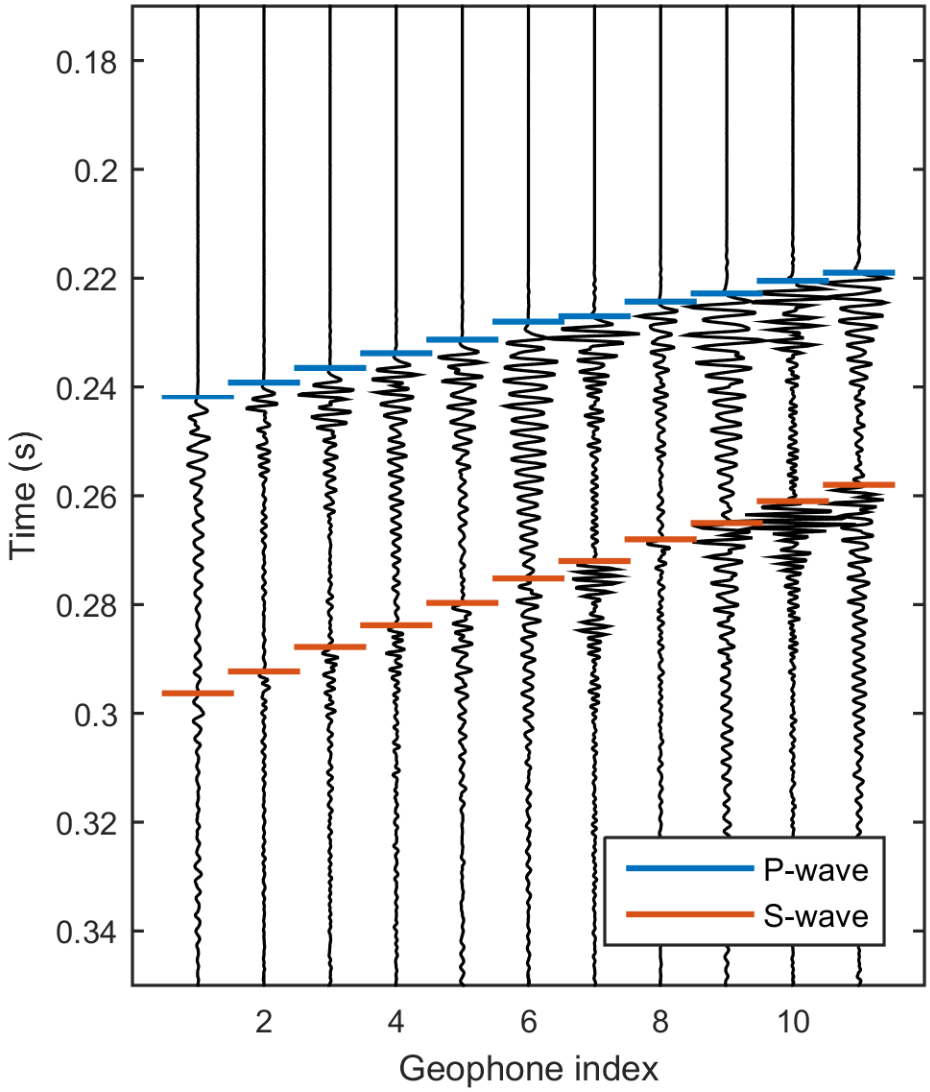

Figure 4-15: Waveforms of a typical perforation shot in stimulation stage 6. The source receiver distance is 0.29 km for geophone 1 and 0.21 km for geophone 11. This perforation shot is near the observation geophone array; thus, the head wave arrives after the direct P-wave arrival. Therefore, we cannot identify the head wave arrival in the waveform.

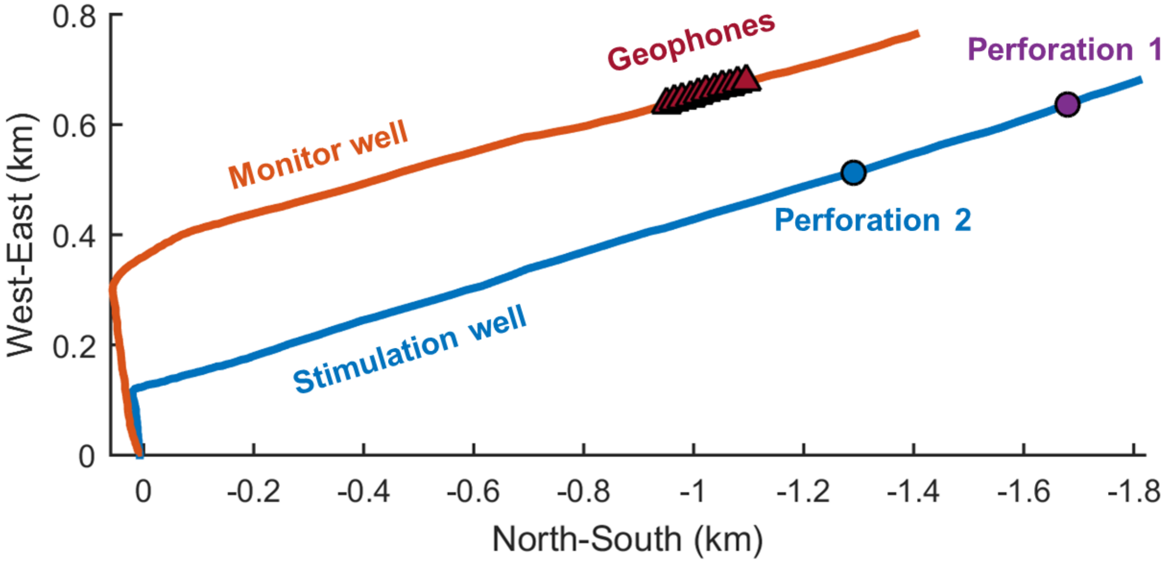

Figure 4-16: The locations of two perforation shots whose waveforms are shown by Figure 4-8 and Figure 4-15.

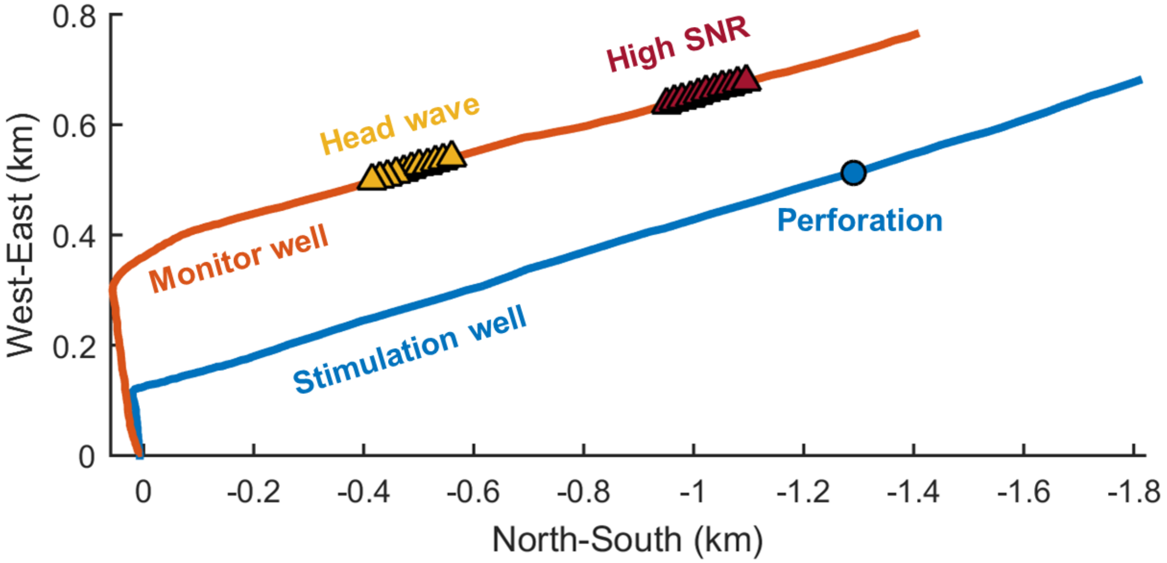

Figure 4-17: Traditional acquisition geometry aims at improving SNR by decreasing source receiver distance (red geophone array). Our study shows that one can monitor hydraulic stimulation with geophone array that is farther than a cross-over distance (yellow geophone array) for head wave observation. This acquisition practice will be able to avoid large location uncertainty due to using P-wave polarization.

4.6 Conclusions

We studied the microseismic signal from a survey in the Marcellus shale. Severe resonances due to reasons such as poor geophone-borehole coupling are identified in the downhole microseismic dataset from preliminary analysis. STFT analysis shows the resonance frequency varies according to geophone channels. We designed a spiking deconvolution filter according to the recorded signals for each channel. The deconvolution is successful in removing resonance and improves the identification of multiple arrivals. However, it won't help to improve the P-wave polarization estimation, which is traditionally used to constrain microseismic event location in single monitoring well observation. The existence of head wave in microseismic survey of Marcellus shale is observed and verified. The location result of perforation shots using the developed method verified that accounting for head wave arrival time as a substitution for P-wave polarization indeed improves the microseismic location accuracy. The relocation result on microseismic events in stage 2 shows a more reasonable pattern than the original catalog estimated with the traditional location method. Based on the developed method, we propose an improved acquisition geometry for single horizontal well hydraulic fracturing monitoring, which enables us to improve the identification of multiple arrivals, thus, improve microseismic event location accuracy as well as reduce acquisition cost.

CHAPTER 5 CONCLUSIONS

5.1 Discussions

Velocity model is usually a major source of uncertainty for microseismic event location problem. However, depending on the setup of a survey, various factors may dominate the location errors. The statics may cause a problem for highly weathered area in a surface microseismic survey. The orientations of geophones may need to be determined in cases where no perforation shot is available. Anisotropy may need to be considered for some specific sites. Thanks to the power of Bayesian inference, these factors may be accounted as model parameters depending on the necessity of a specific survey and availability of observations. The inclusion of these crucial parameters in the model to be estimated reduce the risk of bias introduced by inaccurate models. Also, various observations, such as P-wave polarization, shear wave splitting, reflected and refracted waves, can be used to help improve microseismic event location accuracy. The consideration of these factors should be on a case by case basis depending on the specific situation and data quality of a survey.

In microseismic processing, a data dependent earth model may be necessary due to either fracturing induced time-lapse change or horizontal heterogeneity of the formation. Simultaneous inversion provides the potential to construct data dependent velocity models given the abundance of microseismic events in most surveys. Integrated with rock physics models, the difference between various models can be used to characterize hydrofracture properties or horizontally heterogeneity of the formation. It may also be used to validate or calibrate a rock physics model for fractured rocks.

Due to the anisotropic nature of shale and the potential anisotropy introduced by hydraulic fracturing, the anisotropy parameters may be necessary to be included in the earth model. Indeed, we have observed some clear shear wave splitting phenomena in the microseismic waveforms. This can make the isotropic assumption in this work, as well as the most commonly adopted practice of using isotropic models in microseismic processing, questionable. Preliminary research about anisotropic earth model parameters estimation have been carried out by Li, Zhang, Rodi and Toksoz (2013) with a VTI model and by Grechka, Singh and Das

(2011) with homogeneous orthorhombic model. The simultaneous inversion method used in this paper can also be used for the estimation of anisotropy parameters with microseismic data, which will be one of our future works.

Downhole microseismic monitoring of hydraulic fracturing is challenging in that the limited azimuthal coverage and low SNR are very common. Resonance due to poor geophone-borehole coupling is one of these challenges. A major focus of this work is to draw people's attention to this resonance issue, which would otherwise severely affect the waveform information of the microseismic data. In addition to deconvolution, various techniques should be developed and applied to microseismic signal processing to extract the most valuable information from the commonly noisy microseismic data.

The resonance of geophones, as well as low SNR, makes the usage of P-wave polarization information difficult. Head wave incorporation is a way to constrain the microseismic event location to overcome the azimuthal ambiguity issue. Other phases, such as reflection (Belayouni, Gesret, Daniel and Noble, 2015), may also be used to improve microseismic event location accuracy whenever available. Microseismic monitoring of the hydraulic stimulation at a distance greater than the cross-over distance makes the identification possible. Moreover, it has the potential to improve the identification of other seismic phases since the arrival time difference for different phases will be larger when the source receiver distance is larger.

5.2 Conclusions

In conclusion, we used multiple arrivals to improve microseismic event location accuracy. The usage of multiple arrivals of multiple microseismic data enables the construction of velocity model using only microseismic data. We built the framework for simultaneous inversion of multiple microseismic data for event location and velocity model parameter estimation with Bayesian inference. MAP estimation and the covariance matrix under the Gaussian assumption give an efficient and reasonable approximation to the posterior probability distribution. In addition, Bayesian inference enables the uncertainty to be quantified. The application of the developed location algorithm on a synthetic example and the Newberry EGS data shows that we can successfully construct a velocity model from microseismic data as well as estimate the microseismic event locations. The synthetic study shows that the location uncertainty is typically large in the vertical direction due to the limitation of the acquisition geometry, and the situation is worse as the event goes deeper. Implementation on real microseismic data from the Newberry EGS system shows the possibility of constructing a velocity model purely from microseismic data. With the effective velocity model conforming to the microseismic data, we were able to estimate the microseismic event locations without prior knowledge of the earth model.

The study of the microseismic data from a survey in the Marcellus shale was carried out. It shows the presence of severe resonances due to reasons such as poor geophone-borehole coupling. STFT analysis shows the resonance frequency varies according to geophone channels. We designed a spiking deconvolution filter according to the recorded signals for each channel. The deconvolution is successful in removing resonance and improves the identification of multiple arrivals. However, it won't help to improve the P-wave polarization estimation, which is traditionally used to constrain microseismic event location in single monitoring well observation. The existence of head wave in microseismic survey of Marcellus shale is observed and verified. The location result of perforation shots using the developed method verified that accounting for head wave arrival time as a substitution for P-wave polarization indeed improves the microseismic location accuracy. The relocation result on microseismic events in stage 2 shows a more reasonable pattern than the original catalog estimated with the traditional location method. Based on the developed method, we propose an improved acquisition geometry for single horizontal well hydraulic fracturing monitoring, which enables us to improve the identification of multiple arrivals, thus, improve microseismic event location accuracy as well as reduce acquisition cost.

5.3 Future work

Current microseismic research focuses on the characterization of microseismic events themselves. Our simultaneous inversion result shows the abundance of microseismic events in a typical survey makes the characterization of earth model possible. Thus, it is promising to monitor changes in rock properties introduced by hydraulic stimulation with microseismic signal. The next step of my work is to build time-lapse earth model with field microseismic data, and to characterize hydrofractures with rock physics models explaining the observed changes. This will complement the current microseismic technology of earthquake characterization, and also, make additional use of the microseismic data acquired during a survey. The characterization of reservoir with microseismic data will provide a new approach to make use of microseismic data, that is, understanding the rock property changes due to hydrofractures. The inclusion of rock physics model enables the estimation of various fracture parameters, such as fracture pressure, aspect ratio, and fracture porosity, that are important for hydraulic fracturing appraisal and production prediction. We expect the future research to find a promising way to contribute hydrofracture characterization with microseismic data.

REFERENCES

Aki, K., and P. G. Richards, 1980, Quantitati6e Seismology: Theory and Methods: WH Freeman and Company, San Francisco.

Artman, B., I. Podladtchikov, and B. Witten, 2010, Source location using time ‐ reverse imaging: Geophysical Prospecting, **58**, 861-873.

Artman, B., and B. Witten, Year, Wave-equation microseismic imaging and event selection in the image domain: 2011 SEG Annual Meeting, Society of Exploration Geophysicists.

Belayouni, N., A. Gesret, G. Daniel, and M. Noble, 2015, Microseismic event location using the first and reflected arrivals: Geophysics, **80**, WC133-WC143.

Ciezobka, J., D. Maity, and I. Salehi, Year, Variable Pump Rate Fracturing Leads to Improved Production in the Marcellus Shale: SPE Hydraulic Fracturing Technology Conference, Society of Petroleum Engineers.

Ciezobka, J., and I. Salehi, Year, Controlled hydraulic fracturing of naturally fractured shales–a case study in the Marcellus shale examining how to identify and exploit natural fractures: Paper SPE 164524 presented at the SPE Unconventional Resources Conference, The Woodlands, Texas, USA, 10-12.

Cipolla, C., S. Maxwell, M. Mack, and R. Downie, Year, A practical guide to interpreting microseismic measurements: SPE/EAGE European Unconventional Resources Conference & Exhibition-From Potential to Production.

Cladouhos, T. T., S. Petty, Y. Nordin, M. Moore, K. Grasso, M. Uddenberg, M. Swyer, B. Julian, and G. Foulger, Year, Microseismic monitoring of Newberry Volcano EGS demonstration: Proceedings of the 38th Workshop on Geothermal Reservoir Engineering, Stanford, CA, 11-13.

Claerbout, J. F., 1992, Earth soundings analysis: Processing versus inversion: Blackwell Scientific Publications Cambridge, Massachusetts, USA.

Dong, W., and M. N. Toksöz, 1995, Borehole seismic-source radiation in layered isotropic and anisotropic media: Real data analysis: Geophysics, **60**, 748-757.

Douglas, A., 1967, Joint epicentre determination: Nature, **215**, 47-48.

Dreger, D., R. Uhrhammer, M. Pasyanos, J. Franck, and B. Romanowicz, 1998, Regional and far-regional earthquake locations and source parameters using sparse broadband networks: A test on the Ridgecrest sequence: Bulletin of the Seismological Society of America, **88**, 1353-1362.

Drew, J. E., H. D. Leslie, P. N. Armstrong, and G. Michard, Year, Automated microseismic event detection and location by continuous spatial mapping: SPE Annual Technical Conference and Exhibition, Society of Petroleum Engineers.

Duncan, P., and L. Eisner, 2010, Reservoir characterization using surface microseismic monitoring: Geophysics, **75**, 75A139-175A146.

Eisner, L., P. M. Duncan, W. M. Heigl, and W. R. Keller, 2009, Uncertainties in passive seismic monitoring: The Leading Edge, **28**, 648-655.

Eisner, L., and J. H. Le Calvez, Year, New Analytical Techniques To Help Improve Our Understanding of Hydraulically Induced Microseismicity and Fracture Propagation: SPE Annual Technical Conference and Exhibition, Society of Petroleum Engineers.

Gaiser, J. E., T. J. Fulp, S. G. Petermann, and G. M. Karner, 1988, Vertical seismic profile sonde coupling: Geophysics, **53**, 206-214.

Gesret, A., N. Desassis, M. Noble, T. Romary, and C. Maisons, 2015, Propagation of the velocity model uncertainties to the seismic event location: Geophysical Journal International, **200**, 52-66.

Grechka, V., and A. A. Duchkov, 2011, Narrow-angle representations of the phase and group velocities and their applications in anisotropic velocity-model building for microseismic monitoring: Geophysics, **76**, WC127-WC142.

Grechka, V., P. Singh, and I. Das, 2011, Estimation of effective anisotropy simultaneously with locations of microseismic events: Geophysics, **76**, WC143-WC155.

Hayles, K., R. L. Horine, S. Checkles, and J. Blangy, Year, Comparison of microseismic results from the Bakken Formation processed by three different companies: Integration with surface seismic and pumping data: 81st Annual International Meeting: SEG, Expanded Abstracts.

Jansky, J., V. Plicka, and L. Eisner, 2010, Feasibility of joint 1D velocity model and event location inversion by the neighbourhood algorithm: Geophysical Prospecting, **58**, 229-234.

Kalman, R. E., 1960, A new approach to linear filtering and prediction problems: Journal of basic Engineering, **82**, 35-45.

King, G. E., Year, Hydraulic fracturing 101: what every representative, environmentalist, regulator, reporter, investor, university researcher, neighbor and engineer should know about estimating frac risk and improving frac performance in unconventional gas and oil wells: SPE hydraulic fracturing technology conference, Society of Petroleum Engineers.

Li, J., C. Li, S. A. Morton, T. Dohmen, K. Katahara, and M. N. Toksöz, 2014, Microseismic joint location and anisotropic velocity inversion for hydraulic fracturing in a tight Bakken reservoir: Geophysics, **79**, C111-C122.

Li, J., H. Zhang, W. L. Rodi, and M. N. Toksoz, 2013, Joint microseismic location and anisotropic tomography using differential arrival times and differential backazimuths: Geophysical Journal International, **195**, 1917-1931.

Li, L., and B. Jafarpour, 2010, Effective solution of nonlinear subsurface flow inverse problems in sparse bases: Inverse Problems, **26**, 105016.

Matzel, E., D. Templeton, A. Petersson, and M. Goebel, 2014, Imaging the Newberry EGS Site using Seismic Interferometry.

Maxwell, S., 2009, Microseismic location uncertainty: CSEG Recorder, **34**, 41-46.

Maxwell, S., 2010, Microseismic: Growth born from success: The Leading Edge, **29**, 338-343.

Maxwell, S., 2014, Microseismic imaging of hydraulic fracturing: Improved engineering of unconventional shale reservoirs.

Maxwell, S., J. Rutledge, R. Jones, and M. Fehler, 2010, Petroleum reservoir characterization using downhole microseismic monitoring: Geophysics, **75**, 75A129-175A137.

Miller, R. G., 1974, The jackknife-a review: Biometrika, **61**, 1-15.

Monteiller, V., J. L. Got, J. Virieux, and P. Okubo, 2005, An efficient algorithm for double‐difference tomography and location in heterogeneous media, with an application to the Kilauea Volcano: Journal of Geophysical Research: Solid Earth, **110**.

Myers, S. C., G. Johannesson, and W. Hanley, 2007, A Bayesian hierarchical method for multiple-event seismic location: Geophysical Journal International, **171**, 1049-1063.

Myers, S. C., G. Johannesson, and W. Hanley, 2009, Incorporation of probabilistic seismic phase labels into a Bayesian multiple-event seismic locator: Geophysical Journal International, **177**, 193-204.

Nava, M. J., J. W. Rector, and Z. Zhang, 2015, Characterization of microseismic source mechanism in the Marcellus shale through analysis in the spectral domain, SEG Technical Program Expanded Abstracts 2015: Society of Exploration Geophysicists, 5069-5073.

Oliver, D. S., N. He, and A. C. Reynolds, Year, Conditioning permeability fields to pressure data: ECMOR V-5th European Conference on the Mathematics of Oil Recovery.

Oliver, D. S., A. C. Reynolds, and N. Liu, 2008, Inverse theory for petroleum reservoir characterization and history matching: Cambridge University Press.

Osborn, W. L., S. Petty, T. T. Cladouhos, J. Iovenitti, L. Nofziger, O. Callahan, D. S. Perry, and P. L. Stern, 2011, Newberry Volcano EGS Demonstration-Phase I Results: AltaRock Energy, Inc., Seattle, WA.

Parra, J., C. Hackert, P.-C. Xu, and H. A. Collier, 2006, Attenuation analysis of acoustic waveforms in a borehole intercepted by a sand-shale sequence reservoir: The Leading Edge, **25**, 186-193.

Parra, J. O., C. L. Hackert, A. W. Gorody, and V. Korneev, 2002, Detection of guided waves between gas wells for reservoir characterization: Geophysics, **67**, 38-49.

Petersson, N. A., and B. Sjogreen, 2013, User's guide to SW4, version 1.0: LLNL-SM-xxyy, Lawrence Livermore National Laboratory.

Petty, S., Y. Nordin, W. Glassley, T. T. Cladouhos, and M. Swyer, Year, Improving geothermal project economics with multi-zone stimulation: results from the Newberry Volcano EGS demonstration: Proceedings of the 38th Workshop on Geothermal Reservoir Engineering, Stanford, CA, 11-13.

Poliannikov, O. V., M. Prange, A. Malcolm, and H. Djikpesse, 2013, A unified Bayesian framework for relative microseismic location: Geophysical Journal International, ggt119.

Poliannikov, O. V., M. Prange, A. E. Malcolm, and H. Djikpesse, 2014, Joint location of microseismic events in the presence of velocity uncertainty: Geophysics, **79**, KS51-KS60.

Rutledge, J. T., and W. S. Phillips, 2003, Hydraulic stimulation of natural fractures as revealed by induced microearthquakes, Carthage Cotton Valley gas field, east Texas: Geophysics, **68**, 441-452.

Slawinski, R. A., and M. A. Slawinski, 1999, On raytracing in constant velocity-gradient media: calculus approach: Can. J. Explor. Geophys, **35**, 24-27.

Song, F., and M. N. Toksöz, 2011, Full-waveform based complete moment tensor inversion and source parameter estimation from downhole microseismic data for hydrofracture monitoring: Geophysics, **76**, WC103-WC116.

Tan, Y., C. Chai, and T. Engelder, 2014, Use of S-wave attenuation from perforation shots to map the growth of the stimulated reservoir volume in the Marcellus gas shale: The Leading Edge, **33**, 1090-1096.

Tarantola, A., 2005, Inverse problem theory and methods for model parameter estimation: siam.

Tarantola, A., and B. Valette, 1982, Inverse problems= quest for information: J. geophys, **50**, 150-170.

Templeton, D. C., G. Johannesson, and S. C. Myers, 2014, An Investigation of the Microseismicity at the Newberry EGS Site: Lawrence Livermore National Laboratory (LLNL), Livermore, CA.

Waldhauser, F., and W. L. Ellsworth, 2000, A double-difference earthquake location algorithm: Method and application to the northern Hayward fault, California: Bulletin of the Seismological Society of America, **90**, 1353-1368.

Warpinski, N., 2009, Microseismic monitoring: Inside and out: Journal of Petroleum Technology, **61**, 80-85.

Yilmaz, Ö., 2001, Seismic data analysis: Society of exploration geophysicists Tulsa.

Yilmaz, Ö., 2001, Seismic data analysis: Processing, inversion, and interpretation of seismic data: Society of exploration geophysicists.

Yuan, D., and A. Li, 2016, Determination of microseismic event back azimuth from S-wave splitting analysis, SEG Technical Program Expanded Abstracts 2016: Society of Exploration Geophysicists, 2667-2671.

Yuan, D., R. Stewart, and A. Li, 2016, Joint inversion for anisotropic velocity model and event locations using S-wave splitting measurements from downhole microseismic data, SEG Technical Program Expanded Abstracts 2016: Society of Exploration Geophysicists, 2508-2512.

Zhang, H., S. Sarkar, M. N. Toksöz, H. S. Kuleli, and F. Al-Kindy, 2009, Passive seismic tomography using induced seismicity at a petroleum field in Oman: Geophysics, **74**, WCB57-WCB69.

Zhang, H., and C. Thurber, 2006, Development and applications of double-difference seismic tomography: Pure and Applied Geophysics, **163**, 373-403.

Zhang, H., and C. H. Thurber, 2003, Double-difference tomography: The method and its application to the Hayward fault, California: Bulletin of the Seismological Society of America, **93**, 1875-1889.

Zhang, Z., B. Jafarpour, and L. Li, 2014, Inference of permeability heterogeneity from joint inversion of transient flow and temperature data: Water Resources Research, **50**, 4710-4725.

Zhang, Z., M. Nava, and J. Rector, 2016, Resonance in downhole microseismic data and its removal, SEG Technical Program Expanded Abstracts 2016: Society of Exploration Geophysicists, 2652-2656.

Zhang, Z., J. W. Rector, and M. J. Nava, 2015, Improving microseismic event location accuracy with head wave arrival time: Case study using Marcellus shale, SEG Technical Program Expanded Abstracts 2015: Society of Exploration Geophysicists, 2473-2478.

Zhang, Z., J. W. Rector, and M. J. Nava, 2017, Simultaneous inversion of multiple microseismic data for event locations and velocity model with Bayesian inference: Geophysics, **82**, KS27-KS39.

Zhou, R., L. Huang, and J. Rutledge, 2010, Microseismic event location for monitoring CO 2 injection using double-difference tomography: The Leading Edge, **29**, 208-214.

Zimmer, U., Year, Localization of microseismic events using headwaves and direct waves: 2010 SEG Annual Meeting, Society of Exploration Geophysicists.

Zimmer, U., 2011, Microseismic design studies: Geophysics, **76**, WC17-WC25.